Repression of CTSG, ELANE and PRTN3-mediated histone H3 proteolytic cleavage promotes monocyte-to-macrophage differentiation

Peggie Cheung[1,2,9], Steven Schaffert[1,3,9], Sarah E. Chang[1,2,9], Mai Dvorak[1,2], Michele Donato[1,3], Claudia Macaubas[4], Mariko H. Foecke[1,2], Tie-Mei Li[5], Lichao Zhang[6], John P. Coan[5], Grant S. Schulert[7], Alexei A. Grom[7], Lauren A. Henderson[8], Peter A. Nigrovic[8], Joshua E. Elias[6], Or Gozani[5], Elizabeth D. Mellins[4 ✉], Purvesh Khatri[1,3 ✉], Paul J. Utz[1,2 ✉] and Alex J. Kuo[1,2 ✉]

Chromatin undergoes extensive reprogramming during immune cell differentiation. Here we report the repression of controlled histone H3 amino terminus proteolytic cleavage (H3ΔN) during monocyte-to-macrophage development. This abundant histone mark in human peripheral blood monocytes is catalyzed by neutrophil serine proteases (NSPs) cathepsin G, neutrophil elastase and proteinase 3. NSPs are repressed as monocytes mature into macrophages. Integrative epigenomic analysis reveals widespread H3ΔN distribution across the genome in a monocytic cell line and primary monocytes, which becomes largely undetectable in fully differentiated macrophages. H3ΔN is enriched at permissive chromatin and actively transcribed genes. Simultaneous NSP depletion in monocytic cells results in H3ΔN loss and further increase in chromatin accessibility, which likely primes the chromatin for gene expression reprogramming. Importantly, H3ΔN is reduced in monocytes from patients with systemic juvenile idiopathic arthritis, an autoinflammatory disease with prominent macrophage involvement. Overall, we uncover an epigenetic mechanism that primes the chromatin to facilitate macrophage development.

Controlled histone proteolysis is evolutionarily conserved from unicellular eukaryotes to humans[1]. Multiple classes of proteases show catalytic activities toward the histone H3 tail, including serine[2,3], cysteine[4], aspartyl[5] and metallo-proteases[6]. Truncation of the highly basic and heavily modified H3 N-terminal tail can alter its electrostatic interaction with DNA[7] and impact chemical modifications with pivotal cell regulatory functions[8]. Proteolytic processing of H3 is frequently elevated during cellular differentiation, such as embryonic stem cell development[4], myogenesis[9] and osteoclastogenesis[6], suggesting its crucial roles in regulating cell fate determination and development.
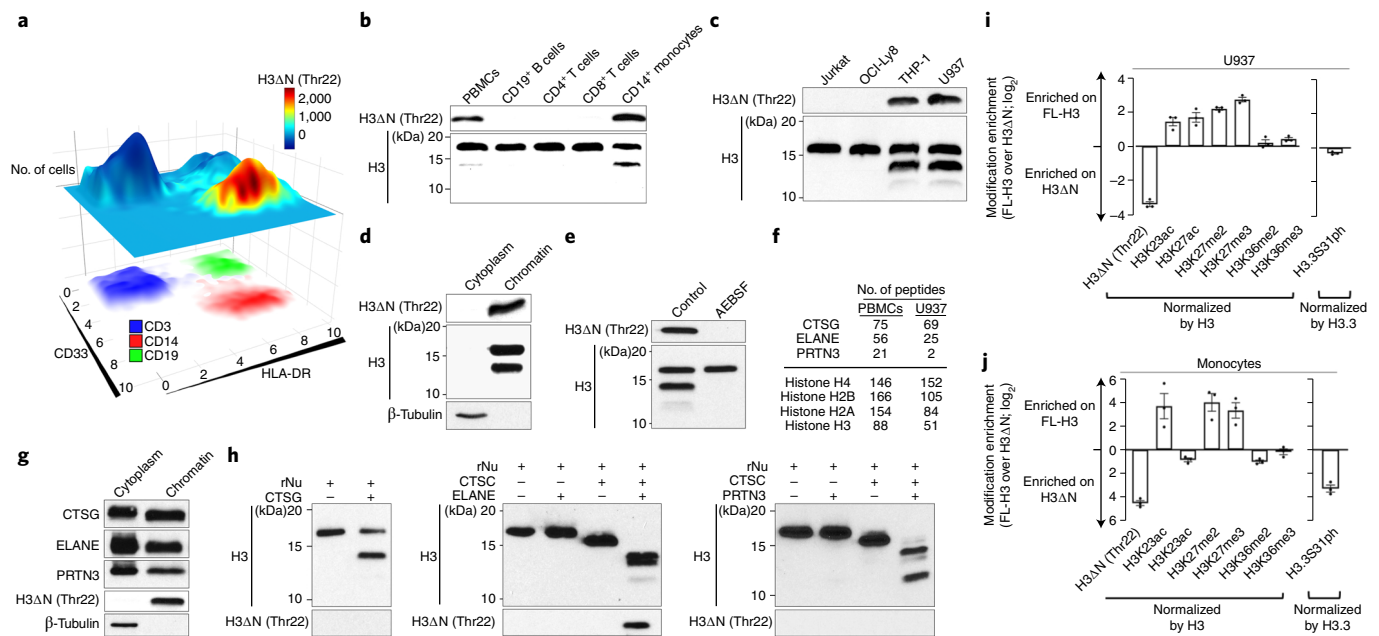
We report that NSPs cathepsin G (CTSG), neutrophil elastase (ELANE) and proteinase 3 (PRTN3) jointly catalyze H3ΔN in monocytes. NSPs are localized to the chromatin, generating H3ΔN that is integrated into nucleosome arrays. During monocyte-to-macrophage differentiation, NSPs and H3ΔN are repressed. Integrative epigenomic analyses reveal H3ΔN association with permissive chromatin and active transcription. Simultaneous ablation of NSPs (ΔNSPs) abolishes H3ΔN but only modestly impacts the transcriptome in the basal condition. Upon phorbol myristate acetate (PMA)-induced differentiation, ΔNSPs cells show a greater response in gene expression. Our data support a model in which chromatin reconfiguration by H3ΔN repression may prime the chromatin to facilitate gene expression

reprogramming during cellular differentiation. Further, H3ΔN is repressed in monocytes from patients with systemic juvenile idiopathic arthritis (sJIA), and the repression is mediated in part by ferritin, a serum protein frequently elevated in patients with sJIA[10,11]. Together, we identify a noncanonical nuclear function of NSPs in epigenetic gene regulation.

Results

CTSG-, ELANE- and PRTN3-mediated H3ΔN in monocytes. Epigenetic landscape profiling using cytometry by time-of-flight (EpiTOF)[12] analysis revealed cell-type-specific enrichment of proteolytically processed histone H3 cleaved between amino acids alanine 21 and threonine 22 (H3ΔNThr22) in HLA-DR+CD33+CD14+ monocytes (Fig. 1a). H3ΔNThr22 was not associated with cell death (Extended Data Fig. 1a), and the enrichment was specific in CD14+CD16− classical monocytes (referred to as 'monocytes' below) but not in CD14+CD16+ intermediate or CD14−CD16+ nonclassical subsets[13] (Extended Data Fig. 1b). At the single-cell level, H3ΔNThr22 abundance is negatively correlated with major histocompatibility complex class II level (Extended Data Fig. 1c). We validated the cell-type-specific enrichment of H3ΔNThr22 in purified monocytes (Fig. 1b). This molecular signature was preserved in monocytic cell lines U937 and THP-1 (Fig. 1c). Biochemical fractionation analysis demonstrated H3ΔN chromatin localization

Fig. 1 | CTSG, ELANE and PRTN3 catalyze H3ΔN in monocytes. a, H3ΔNThr22 distinguishes CD14^{+} monocytes. EpiTOF analysis of PBMCs from 20 healthy volunteers as described previously[12]. x and y axes, HLA-DR and CD33 levels, respectively. Top plane: color, normalized H3ΔNThr22 level; height, cell count. Bottom plane: color, CD3 (blue), CD14 (red) and CD19 (green) levels. **b**, Monocyte-specific H3ΔN enrichment relative to lymphocytes. Western blot analysis of whole-cell extract (WCE) from purified primary human immune cells. **c**, Monocytic cell lines retain high H3ΔN levels in comparison with other cell lines of lymphoid origins. Western blot analysis of WCE from the indicated cell lines. **d**, H3ΔN native chromatin incorporation. Western blot analysis of U937 cells biochemically separated into cytoplasmic and chromatin fractions. **e**, Serine protease–mediated H3ΔN. Western blot analysis of WCE from AEBSF-treated U937 cells. Control, PBS-treated. **f,g**, Chromatin localization of CTSG, ELANE and PRTN3. Protein identification of purified chromatin from PBMCs (left) or U937 cells (right) using mass spectrometry. The numbers of peptides mapped to the indicated histone proteins and serine proteases are shown (**f**). Western blot analysis of cytoplasmic and chromatin fractions purified from U937 cells (**g**). Molecular weight markers, see Source Data. **h**, CTSG, ELANE and PRTN3 catalyze controlled H3 proteolytic cleavage in vitro. Immunoblotting analysis of protease assays using recombinant CTSG (left), ELANE (middle) or PRTN3 (right) and recombinant nucleosomes (rNu) as substrate. ELANE and PRTN3 activities require pre-activation by CTSC[51]. **i,j**, Differential histone modifications between FL-H3 and truncated H3. Quantification of the indicated histone marks between FL-H3 and H3ΔN in U937 cells (**i**) or primary monocytes (**j**). y axis, FL-H3-over-H3ΔN ratio of the indicated histone marks normalized against the ratio of H3 or H3.3 (for H3.3S31ph). Data represent mean ± s.e.m. (three biological replicates).

(Fig. 1d and Extended Data Fig. 1d), suggesting its physiological importance in regulating DNA-templated biological processes.

To identify the protease(s) catalyzing H3ΔN in monocytes, we first tested proteases with known H3-cleaving activities. Depletion of cathepsin L, which processes H3 during mouse embryonic stem cell development[4], did not impact H3ΔN in monocytes (Extended Data Fig. 1e). H3ΔN both in U937 and in THP-1 cells was unaffected by MMP9 inhibition, which targets H3 during osteoclastogenesis (Extended Data Fig. 1f)[6], or E64d, a cell-permeable nonselective cysteine protease inhibitor (Extended Data Fig. 1g)[14]. Strikingly, a broad-spectrum serine protease inhibitor, 4-(2-aminoethyl)benzenesulfonyl fluoride (AEBSF), abolished H3ΔN in monocytic cells (Fig. 1e and Extended Data Fig. 1h). Thus, we limited our search scope to serine proteases present at the chromatin. Protein identification using mass spectrometry found abundant CTSG, ELANE and PRTN3 at the native chromatin isolated from peripheral blood mononuclear cells (PBMCs) and U937 cells (Fig. 1f). Chromatin localization of individual NSPs was validated by immunoblotting (Fig. 1g and Extended Data Fig. 1i). NSPs remained chromatin-bound after extensive washes of chromatin pellet and were solubilized together with histones and HP-1 in a high-salt solution[15] (Extended Data Fig. 1j). Next, in vitro protease assay using NSPs and recombinant nucleosomes[16] showed that all three NSPs demonstrated regulated proteolytic activities towards H3 on the physiological substrate (Fig. 1h). Notably, H3ΔNThr22 was only detected in the protease assay using ELANE and not in others with CTSG or PRTN3, indicating

that ELANE is the only NSP generating H3ΔNThr22 in vitro. Tandem mass spectrometry analysis of protease assay revealed that CTSG preferentially cleaved at Leu20, and PRTN3 primarily catalyzed Lys23 cleavage (Extended Data Fig. 1k). Both ELANE and PRTN3 efficiently catalyzed the cleavage at Thr32. Together, CTSG, ELANE and PRTN3 generate multiple truncated H3 products.

Immunoblotting revealed distinct chemical modification profiles between FL-H3 and H3ΔN in U937 cells (Fig. 1i and Extended Data Fig. 1l) and in primary monocytes (Fig. 1j and Extended Data Fig. 1m). Di- and tri-methylation of H3 at lysine 27 (H3K27me2 and H3K27me3, respectively) were present almost exclusively on FL-H3. In contrast, di- and tri-methylation of H3 at lysine 36 (H3K36me2 and H3K36me3, respectively) were indiscriminately distributed between both H3 forms. In U937 cells, acetylation at lysine 27 (H3K27ac) was also enriched on FL-H3. However, H3K27ac was near evenly distributed between FL-H3 and H3ΔN in primary monocytes. Proteolytic processing also occurred on histone variant H3.3. Phosphorylation at serine 31 (H3.3S31ph) was enriched on H3ΔN in primary monocytes but not in U937 cells. The difference may be due to active cell proliferation of U937 cells[17]. Together, these data suggest crosstalk between H3ΔN and other chemical modifications and its functional importance.

Altered cell morphology and functions upon NSP depletion. CTSG, ELANE and PRTN3 arose from a common ancestor through gene duplication during evolution and remain highly homologous
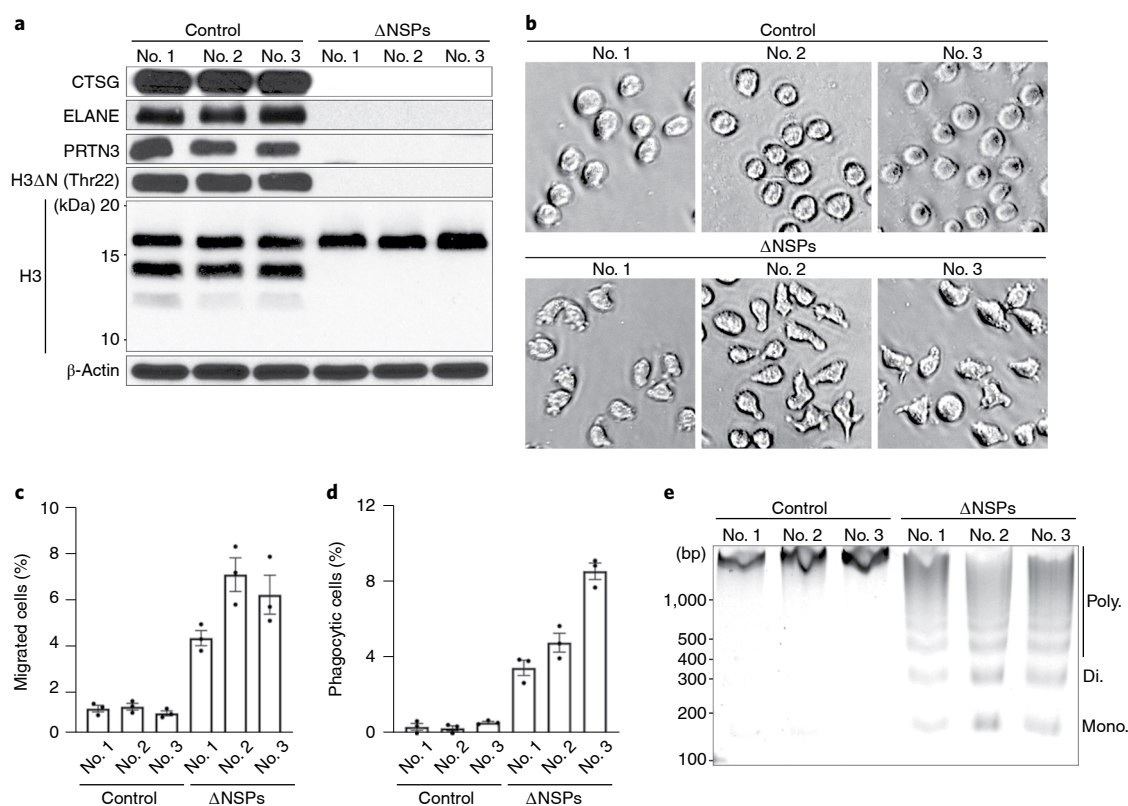
Fig. 2 | Morphologic and functional alterations in monocytic cells ablated of *CTSG*, *ELANE* and *PRTN3*. a, CTSG, ELANE and PRTN3 jointly catalyze H3ΔN in U937 cells. Western blot analysis of WCE from monoclonal U937 cells stably expressing CRISPR–Cas9 and sgRNAs targeting CTSG, ELANE and PRTN3 simultaneously. Control cells express CRISPR–Cas9 without sgRNA. **b**, Morphological alterations of ΔNSPs cells. Representative light microscopy images of ΔNSPs cells as in **a**. **c,d**, Functional alterations of ΔNSPs cells. Transwell cell migration (**c**) and phagocytosis (**d**) analyses of ΔNSPs cells described in **a**. Data represent mean ± s.e.m. (three technical replicates). **e**, Increased sensitivity to MNase digestion upon NSP depletion. MNase sensitivity analysis of the indicated cells. DNA marker and the expected sizes of mono-, di- and poly-nucleosomes are shown.

in primary sequence[18]. Genetic ablation of individual NSPs did not affect H3ΔN (Extended Data Fig. 2a–c), consistent with our in vitro findings. Notably, in agreement with the in vitro data (Fig. 1h), ELANE depletion abrogated H3ΔNThr22 (Extended Data Fig. 2b), indicating that H3ΔNThr22 is generated exclusively by ELANE both in vitro (Fig. 1h, middle) and in cells (Extended Data Fig. 2b). The H3ΔNThr22 antibody used in this study was highly specific, showing negligible cross-reactivity with other H3ΔN species (Extended Data Fig. 2d).

Strikingly, H3ΔN was abolished in three U937 cell clones depleted of CTSG, ELANE and PRTN3 simultaneously (ΔNSPs) (Fig. 2a). Control cells underwent the same viral transduction processing as ΔNSPs clones and were cultured in the presence of an identical set of antibiotics. Clonal selection of control cells did not alter H3ΔN level (Extended Data Fig. 2e), cell morphology (Extended Data Fig. 2f), or CD11b and CD11c expression (Extended Data Fig. 2g). Thus, we used control cells without clonal selection for downstream analyses to preserve potential cellular heterogeneity.

ΔNSPs cells exhibited an irregular shape (Fig. 2b), increased migration ability (Fig. 2c) and phagocytic capability (Fig. 2d). Increased sensitivity to micrococcal nuclease (MNase) digestion in ΔNSPs cells indicated altered global chromatin dynamics in response to NSP depletion (Fig. 2e). Importantly, NSP depletion minimally impacted cell viability (Extended Data Fig. 2h). To determine if the molecular, morphological and functional alterations in ΔNSPs cells were dependent upon H3ΔN loss at chromatin, we established an experimental system to reintroduce H3ΔN into ΔNSPs cells. An epitope-tagged exogenous H3 with a tobacco

etch virus (TEV) protease substrate sequence inserted between Ala21 and Thr22 (H3^ENLYFQS-FLAG) was introduced along with a tetracycline-inducible TEV protease (iTEV) into ΔNSPs cells (Extended Data Fig. 2i). H3^ENLYFQS-FLAG can be electrophoretically resolved from endogenous H3 (Extended Data Fig. 2j). Biochemical fractionation analysis showed H3^ENLYFQS-FLAG chromatin integration (Extended Data Fig. 2k). Upon doxycycline treatment, all cells remained over 93% viable (Extended Data Fig. 2l). We observed an electrophoretically fast-migrating band that matched the molecular weight of N-terminally cleaved H3^ENLYFQS-FLAG (Extended Data Fig. 2m), with the cleavage product representing approximately one-third of exogenous H3. ΔNSPs cells containing cleaved H3^ENLYFQS-FLAG returned to wild-type cell morphology (Extended Data Fig. 2n) and showed reduced migration ability (Fig. 2o) and phagocytosis capability (Fig. 2p). Further, reintroducing H3ΔN into ΔNSPs cells resulted in reduced MNase sensitivity (Extended Data Fig. 2q), suggesting a direct role of H3ΔN in regulating chromatin architecture. While exogenous H3^ENLYFQS-FLAG represents a small fraction of bulk H3, and iTEV protease-mediated proteolysis unlikely recapitulates the endogenous H3ΔN genomic distribution, these data suggest that the morphological and functional phenotypes mimicking macrophages in ΔNSPs cells are regulated, at least in part, by H3ΔN. Moreover, these data also provide direct evidence that H3ΔN affects global chromatin structure.

NSP and H3ΔN repression during macrophage development. Compelling evidence from monocytic cell lines led us to extend our investigation to primary monocytes and monocyte-derived
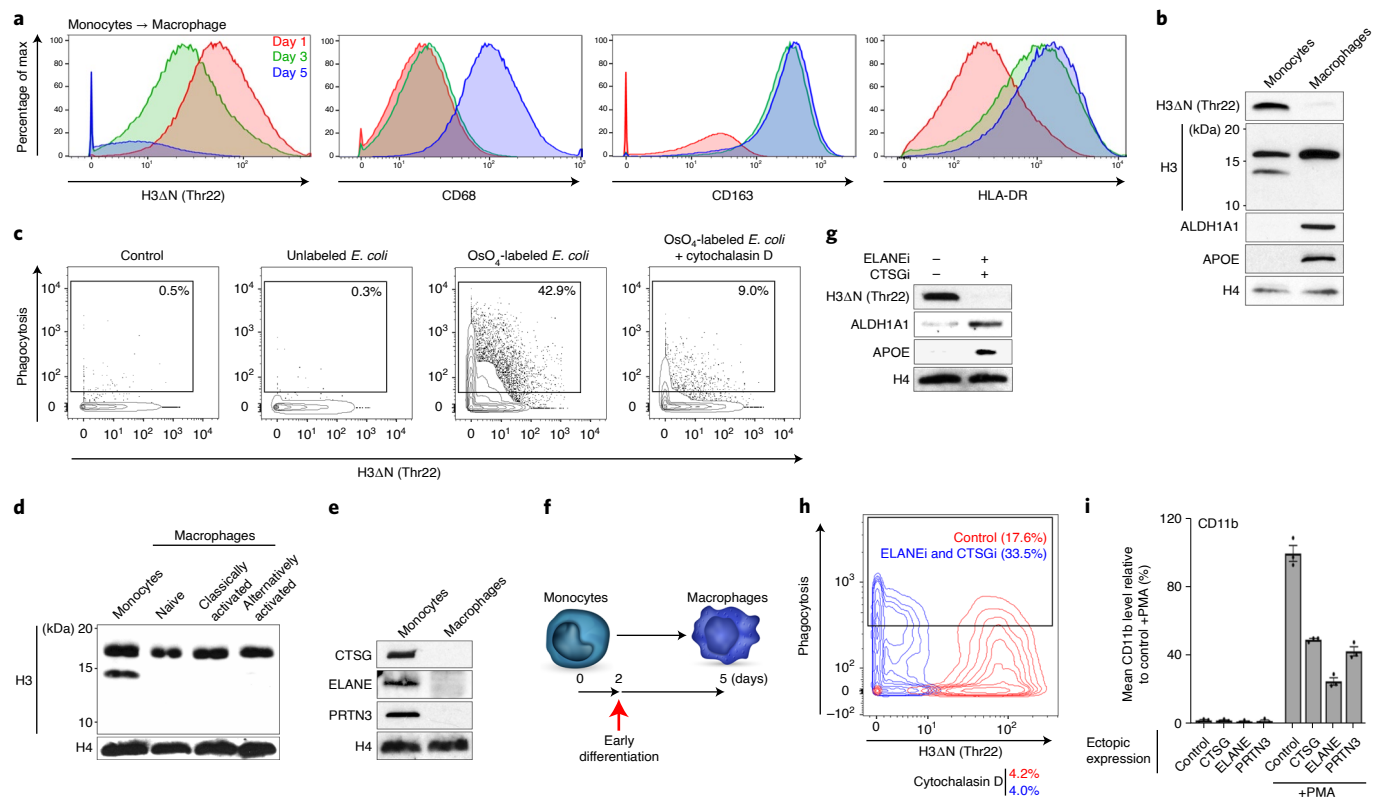
Fig. 3 | NSP and H3ΔN repression during monocyte-to-macrophage differentiation. a,b, H3ΔN repression as monocytes differentiate into macrophages. Mass cytometry (**a**) and western blot (**b**) analyses of primary monocytes and the matching monocyte-derived macrophages. Cells collected at days 1 (red), 3 (green) and 5 (blue) are analyzed by mass cytometry (**a**). Day 1 and day 7 samples are subjected to immunoblotting analysis (**b**). Molecular weight markers, see Source Data. **c**, Increased phagocytosis capability of differentiating monocytes with repressed H3ΔN. Mass cytometry analysis of cells as in **a** (day 5) incubated with osmium-labeled *E. coli* to assess phagocytosis capability[22]. Control, no *E. coli* particle is added; cytochalasin D, control to show the specificity of phagocytosis measurement. H3ΔNThr22 (*x* axis) and osmium (*y* axis) levels measured by mass cytometry are shown. **d**, H3ΔN repression is maintained in polarized macrophages. Western blot analysis of peripheral blood monocytes, naive macrophages generated as in **b**, classically activated macrophages polarized by LPS and IFN-γ, and alternatively activated macrophages polarized by IL-4. **e**, CTSG, ELANE and PRTN3 repression during monocyte-to-macrophage differentiation. Western blot analysis of the samples as in **b** using the indicated antibodies. Molecular weight markers, see Source Data. **f–h**, Accelerated macrophage development by pharmacological inhibition of NSPs. Overview of the chronological timeline for this experiment (**f**). Western blot analysis of WCE from peripheral blood monocytes cultured in the presence or absence of ELANE inhibitor (ELANEi) GW311616 in combination with CTSG inhibitor (CTSGi) CAS 429676-93-7 for 2 d (**g**). Molecular weight markers, see Source Data. Phagocytosis analysis of the cells as in **g** using mass cytometry and osmium-labeled *E. coli* (**h**). **i**, Constitutive NSP expression suppresses monocytic cell differentiation. U937 cells stably expressing the indicated NSPs (*x* axis) under the control of cytomegalovirus promoter are induced for differentiation by PMA. CD11b expression is determined by mass cytometry. Data represent mean ± s.e.m. (three technical replicates).

macrophages[19]. Mass cytometry analysis of monocytes differentiating into macrophages ex vivo revealed time-dependent H3ΔNThr22 loss and elevated CD68, CD163 and HLA-DR expression indicative of macrophage maturation[20,21] (Fig. 3a and Extended Data Fig. 3a). At day 5 after induction for differentiation, H3ΔNThr22 was undetectable in over 70% of cells by mass cytometry. H3ΔNThr22 repression was not associated with cell death (Extended Data Fig. 3b). At day 7, all H3ΔN species were largely undetectable by immunoblotting in fully mature macrophages (Fig. 3b and Extended Data Fig. 3c), indicating that all species of truncated H3 were repressed during macrophage development. Functionally, mature macrophages efficiently engulfed osmium-labeled *Escherichia coli* particles in mass cytometry analysis[22] (Fig. 3c and Extended Data Fig. 3d). Cells with undetectable H3ΔNThr22 showed the greatest degree of phagocytosis, suggesting that the loss of H3ΔNThr22 is indicative of full maturation of macrophages. H3ΔN depletion was maintained in macrophages classically or alternatively activated by lipopolysaccharide (LPS) and interferon-γ (IFN-γ) or interleukin-4 (IL-4), respectively[23] (Fig. 3d and Extended Data Fig. 3e). Moreover, we

found that NSPs were repressed during macrophage differentiation (Fig. 3e and Extended Data Fig. 3f), explaining H3ΔN depletion in mature macrophages. In U937 cells stimulated with PMA to induce macrophage-like phenotypes, NSP transcripts (Extended Data Fig. 3g) and proteins (Extended Data Fig. 3h) were both suppressed. Together, our data demonstrate that NSPs and H3ΔN are repressed as monocytes differentiate into macrophages.

Treatment of primary monocytes with selective CTSG and ELANE inhibitors promoted macrophage development. At day 2 after differentiation was initiated (Fig. 3f), differentiating cells cultured in the presence of CTSG and ELANE inhibitors expressed higher macrophage markers APOE and ALDH1A1 (Fig. 3g and Extended Data Fig. 3i) and demonstrated elevated phagocytosis capability (Fig. 3h and Extended Data Fig. 3j), suggesting accelerated macrophage development. Next, we transduced U937 cells with lentiviral vectors encoding individual NSPs under cytomegalovirus promoter control. Exogenous NSP expression was unaffected by PMA-induced NSP repression during cellular differentiation (Extended Data Fig. 3k). H3ΔN levels were

largely maintained in these modified cell lines where a single NSP remained highly expressed. Ectopic overexpression of individual NSPs suppressed CD11b (Fig. 3i) and CD11c (Extended Data Fig. 3l) expression by as much as 70% upon PMA-induced differentiation. Together, these data suggest critical roles for NSPs in regulating monocyte-to-macrophage differentiation.

Widespread H3ΔN genomic distribution at accessible chromatin. To characterize the molecular functions of H3ΔN in monocytes, we adopted an integrative epigenomic approach, performing chromatin immunoprecipitation followed by high-throughput sequencing (ChIP–seq) on H3ΔNThr22 and bulk H3 in wild-type U937 cells, with paired assay for transposase-accessible chromatin using sequencing (ATAC-seq) and RNA sequencing (RNA-seq) on ΔNSPs and control cells. Affinity reagents were validated for ChIP–seq application (Extended Data Fig. 4a). H3ΔNThr22 immunoprecipitation of sheared chromatin containing predominantly mono-nucleosomes (Extended Data Fig. 4b) modestly enriched for the fast-migrating band observed in immunoblotting (Extended Data Fig. 4a), suggesting that a large proportion of immunoprecipitated nucleosomes may be asymmetrically cleaved at H3. Under a 5% irreproducible discovery rate (IDR)[24] cutoff, we identified 15,504 peaks enriched with H3ΔNThr22 consistent between both biological replicates (Fig. 4a). H3ΔNThr22 peaks were dispersed across the genome (Extended Data Fig. 4c), with preferential enrichment in genic over intergenic regions (Fig. 4b). In total, 9,540 genes were found to have one or more H3ΔNThr22 peaks, mostly in promoters, exons and untranslated regions (UTRs). Quantitative PCR (qPCR) analysis validated ChIP–seq findings (Fig. 4c,d and Extended Data Fig. 4d,e). The signals were specific as they were nearly undetectable in ΔNSPs cells. Surprisingly, at the loci where H3ΔNThr22 ChIP–seq signals were low, we also detected considerable H3ΔNThr22 enrichment in control cells. These data indicate that while H3ΔNThr22 is enriched at specific genomic sites, particular in genic regions, it is also widely distributed at a low level across the genome. Moreover, antibodies against NSPs co-immunoprecipitated nucleosomal H3 under the stringent chromatin immunoprecipitation (ChIP) condition, further supporting NSP chromatin localization (Extended Data Fig. 4f). ChIP analysis using an antibody against ELANE, which is the sole NSP catalyzing H3ΔNThr22 in cells (Extended Data Fig. 2b), revealed its presence at loci with both high and low H3ΔNThr22 enrichment (Fig. 4d and Extended Data Fig. 4e). The signals were specific as they were largely undetectable in ΔNSPs cells. These data suggest widespread ELANE occupancy across the genome and that site-specific H3ΔNThr22 enrichment is controlled by mechanisms other than ELANE genomic localization.

To investigate the relationship between H3ΔNThr22 enrichment and chromatin accessibility, we overlaid the H3ΔNThr22 ChIP–seq genomic track over the ATAC-seq datasets from control cells. We performed a cross-correlation analysis at the nucleotide level. We discovered a positive correlation between H3ΔNThr22 ChIP–seq and ATAC-seq signals at individual nucleotides (Fig. 4e), with the highest correlation observed as the overlay was shifted by approximately 250 base pairs (bp) up- or downstream. The offset suggests accessible sequences surrounding H3ΔNThr22-containing nucleosomes. With a 5% false discovery rate (FDR) cutoff, we identified 94,615 ATAC-seq peaks in control cells. H3ΔNThr22 ChIP–seq and ATAC-seq peaks were highly concordant (Fig. 4f and Extended Data Fig. 4g). In total, 78.3% of H3ΔNThr22 peaks (Fig. 4a) were associated with one or more of these accessible sites (Fig. 4g). Moreover, H3ΔNThr22 was strongly enriched at the transcriptional start site (TSS) of actively transcribed genes relative to those with medium or low expression (GSE107566 (ref. [25])) (Fig. 4h and Extended Data Fig. 4h). Together, these data demonstrate H3ΔNThr22 enrichment at permissive chromatin and its positive correlation with gene expression.

Next, we extended the epigenomic analysis to primary monocytes and the matching monocyte-derived macrophages. We isolated peripheral blood monocytes from three healthy volunteers (Extended Data Fig. 5a) and generated monocyte-derived macrophages[19]. The differentiation was confirmed by increased CD68 expression (Extended Data Fig. 5b) and other macrophage markers (Fig. 3a and Extended Data Fig. 3a). Three sets of paired monocytes and macrophages were subject to ChIP–seq analysis of H3ΔNThr22 and bulk H3. The peak-calling algorithm[26] identified 4,851, 8,617 and 11,807 peaks in the three monocyte samples using an FDR 5% cutoff (Fig. 5a). In total, 6,150 H3ΔNThr22 peaks were shared between two or three donors, which we used for downstream analyses. Strikingly, under the same 5% FDR threshold, 0, 282 and 1 H3ΔNThr22 peaks were significant in macrophages from the three donors, respectively. H3ΔNThr22 distribution was widespread in monocytes (Extended Data Fig. 5c) with genic region enrichment (Fig. 5b). A total of 5,011 genes contained one or more H3ΔNThr22 peaks, including transcription factor PU.1 (SPI1) (Fig. 5c) and the p65 (RELA) subunit of NF-κB (Extended Data Fig. 5d). qPCR analysis validated H3ΔNThr22 enrichment at ChIP–seq peaks (Fig. 5d and Extended Data Fig. 5e). At loci with low H3ΔNThr22 ChIP–seq signals in monocytes, we detected considerable H3ΔNThr22, suggesting H3ΔNThr22 presence at a low level across the genome. The ChIP signals were specific as nearly no H3ΔNThr22 was detected in mature macrophages. ELANE occupancy was observed at loci with both high and low H3ΔNThr22, indicating mechanisms other than ELANE localization in controlling H3ΔNThr22 genomic distribution. Overall, the H3ΔNThr22 genomic distribution in primary monocytes is highly similar to that in U937 cells.

To investigate the relationship between H3ΔNThr22 enrichment and chromatin accessibility in primary cells, we leveraged a publicly available ATAC-seq dataset from purified monocytes (GSE87218 (ref. [27])). Using a 5% FDR cutoff, we found a high degree of peak concordance between both datasets in the greater genomic regions surrounding PU.1 and RELA (Fig. 5e and Extended Data Fig. 5f). Strikingly, 96.5% of H3ΔNThr22 ChIP–seq peaks were associated with one or more ATAC-seq peaks (Fig. 5f). Actively transcribed genes showed the highest H3ΔNThr22 level in their TSS-proximal regions (GSE5099 (ref. [19])) (Fig. 5g). These data provide strong support for H3ΔNThr22 enrichment at open chromatin and actively transcribed genes in primary monocytes. Together, integrative analyses of ChIP–seq and ATAC-seq datasets from primary monocytes reveal H3ΔNThr22 association with permissive chromatin and active transcription, a pattern similar to that observed in U937 cells.

Chromatin priming mediated by NSP and H3ΔN repression. Transcriptomic analysis by RNA-seq discovered modest gene expression changes between ΔNSPs and control cells (Fig. 6a), with 170 and 220 genes up- or downregulated in ΔNSPs relative to control cells under a 5% FDR cutoff, respectively. Integrative analysis with the ATAC-seq dataset found increased chromatin accessibility at genes upregulated in ΔNSPs cells (Extended Data Fig. 6a), whereas the chromatin at downregulated genes became inaccessible. Gene ontology analysis revealed that genes upregulated upon NSP and H3ΔN depletion were involved in immune regulation (GO:0002376, $P < 6.8 \times 10^{-06}$; GO:0002684, 5.3×10^{-04}) (Extended Data Fig. 6b), including AIF1, CXCL8/IL8, GPR183/EBI2, ID2, JUN and JUNB which have been linked to macrophage development and polarization. Upregulation of these genes is in agreement with the morphological and functional alterations in ΔNSPs cells (Fig. 2b–d). Importantly, reintroduction of H3ΔN into ΔNSPs cells repressed the expression of these genes (Fig. 6b). These data support a direct role of H3ΔN in transcriptional regulation and that H3ΔN repression affects genes regulating macrophage-associated phenotypes.
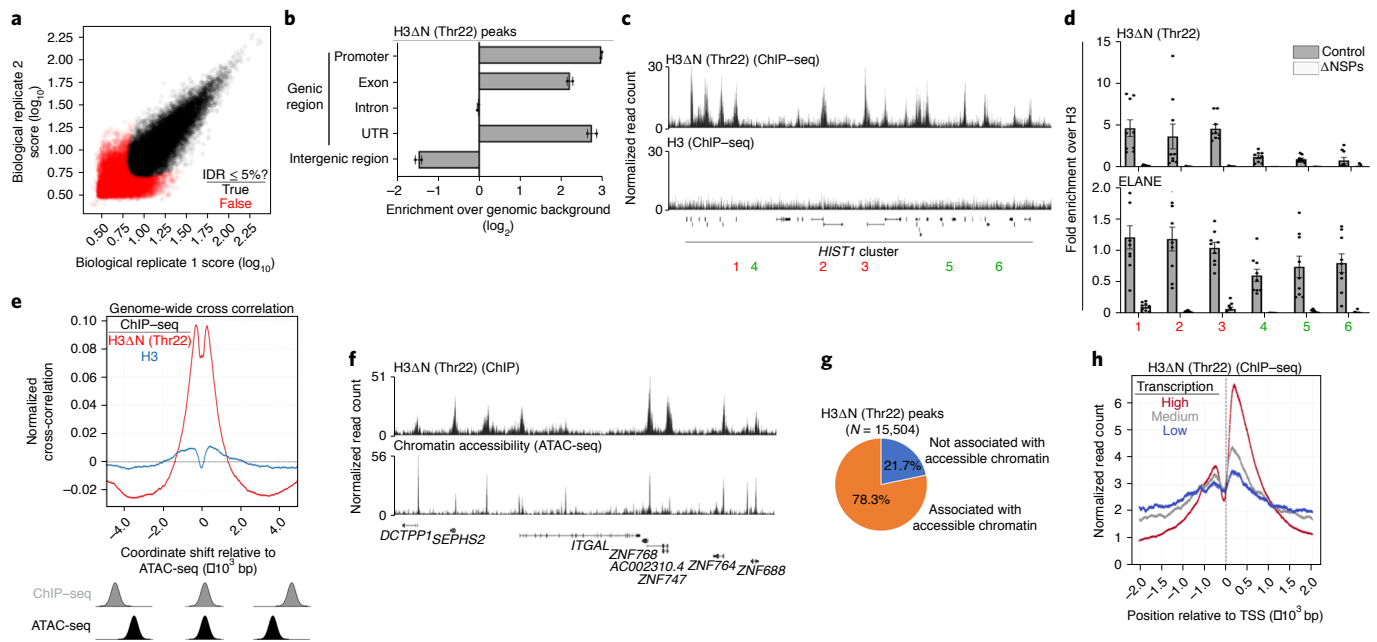
Fig. 4 | Widespread H3ΔN genomic distribution and its permissive chromatin association in monocytic cells. a, Identification of H3ΔNThr22-enriched peaks in wild-type U937 cells. Scaled signal intensities of H3ΔNThr22 ChIP–seq peaks in biological replicates one (*x* axis) and two (*y* axis). Peaks that pass the 5% IDR[24] threshold are labeled (black). Red, peaks with IDR > 5%. **b**, Genic region enrichment of H3ΔNThr22. *x* axis, the enrichment of H3ΔNThr22 peaks in the indicated genomic regions. Center line, genomic distribution with no enrichment. Data represent mean ± s.d. (two biological replicates). **c,d**, H3ΔNThr22 enrichment and ELANE occupancy at the HIST1 locus. Representative genomic tracks of H3ΔNThr22 (top) and bulk H3 (bottom) ChIP–seq data. Regions with high (red) or low (green) H3ΔNThr22 are tested (**c**). qPCR analysis of H3ΔNThr22 (top) or ELANE (bottom) ChIP DNA from control (gray) or ΔNSPs (white) cells using the indicated primer pairs. *y* axes, fold enrichment over signals from bulk H3. Data represent mean ± s.e.m. (three biological replicates (three control cell lines or three ΔNSPs clones) with three technical replicates (*N* = 9)) (**d**). **e**, Association between H3ΔNThr22 enrichment and permissive chromatin at the nucleotide level. Cross-correlation analysis that overlays the H3ΔNThr22 (red) or bulk H3 (blue) ChIP–seq datasets over the ATAC-seq dataset. Aggregate data from 1,000 randomly selected start points are shown. Correlations are computed as the ChIP–seq datasets are shifted with a distance in base pairs depicted at the *x* axis relative to the ATAC-seq dataset. *y* axis, normalized correlation score. **f,g**, Association between H3ΔNThr22 enrichment and permissive chromatin at the peak level. Representative genomic tracks of H3ΔNThr22 ChIP–seq (top) and ATAC-seq (bottom) datasets (**f**). Pie chart depicts the percentage of H3ΔNThr22 ChIP–seq peaks that are associated with ATAC-seq peaks (**g**). **h**, Association between H3ΔNThr22 enrichment and active transcription. H3ΔNThr22 levels at the TSS-proximal regions of genes with high (red), medium (gray) or low (blue) transcription activities (GSE107566 (ref. [25])). *x* axis, base pairs relative to TSS; *y* axis, H3ΔNThr22 ChIP–seq signal intensity.

Across the genome, differential analysis of ATAC-seq data between ΔNSPs and control cells identified 25,900 peaks with increased chromatin accessibility in ΔNSPs over control cells (Fig. 6c). In contrast, under the same FDR 5% threshold, only 16 peaks showed decreased accessibility in ΔNSPs cells relative to controls. Differentially accessible peaks in ΔNSPs cells were dispersed across the genome (Extended Data Fig. 6c) with enrichment in genic regions (Extended Data Fig. 6d). Specifically, among the 15,504 H3ΔNThr22-enriched peaks in wild-type U937 cells (Fig. 4a), 9,654 were associated with differential ATAC-seq peaks in ΔNSPs cells (Fig. 6d), suggesting increased chromatin accessibility upon H3ΔNThr22 depletion. Of these 9,654 peaks, 85.8% were already maintained at a permissive chromatin state in control cells (Fig. 6e,f, and Extended Data Fig. 6e). In summary, NSP depletion greatly impacts chromatin dynamics, resulting in a global increase in chromatin accessibility. At H3ΔNThr22-enriched loci in wild-type cells, we observed further increase in accessibility upon NSP and H3ΔNThr22 depletion.

However, dramatic alterations in chromatin accessibility were only associated with modest gene expression changes (Fig. 6a). We hypothesize that the increased chromatin accessibility in response to H3ΔN repression may represent a potentiated chromatin state, which facilitates gene expression reprogramming in the presence of external cues for differentiation. A permissive chromatin state was found in ΔNSPs cells at genes encoding proinflammatory cytokines

and key immune modulators, such as IL-1β, tumor-necrosis factor-α (TNF-α), macrophage inflammatory protein-1α (MIP-1α), MIP-1β, IL-18, lymphotoxin-α, IL-10 and TNFR2 (Extended Data Fig. 7a). Loci encoding cell adhesion molecules CD11b and CD11c also showed increased chromatin accessibility in cells depleted of NSPs (Extended Data Fig. 7b). While the transcription activities of these genes were not significantly affected by the increased chromatin accessibility in ΔNSPs cells in the basal condition (Fig. 6a), upon PMA-induced differentiation, ΔNSPs cells responded with a higher magnitude of proinflammatory cytokine and immune modulator secretion (Fig. 7a) and expressed higher CD11b and CD11c relative to control cells (Fig. 7b). In addition to genes upregulated upon PMA stimulation, ΔNSPs cells also responded to PMA with a greater degree of transcriptional repression for genes downregulated during differentiation (GSE107566 (ref. [25])) (Fig. 7c). These genes were also enriched with H3ΔNThr22 in wild-type U937 cells and showed elevated chromatin accessibility in ΔNSPs relative to control cells (Extended Data Fig. 7c).

To determine H3ΔN involvement in these transcriptional effects, we treated ΔNSPs cells into which H3ΔN was reintroduced (Extended Data Fig. 2m) with PMA to induce cellular differentiation mimicking macrophage development. The presence of H3ΔN in ΔNSPs cells attenuated *CCL7*, *MMP9*, *TNF-α*, *CD11B* and *CD11C* upregulation (Fig. 7d, top) upon PMA-induced cell differentiation, in addition to the repression of genes downregulated during this
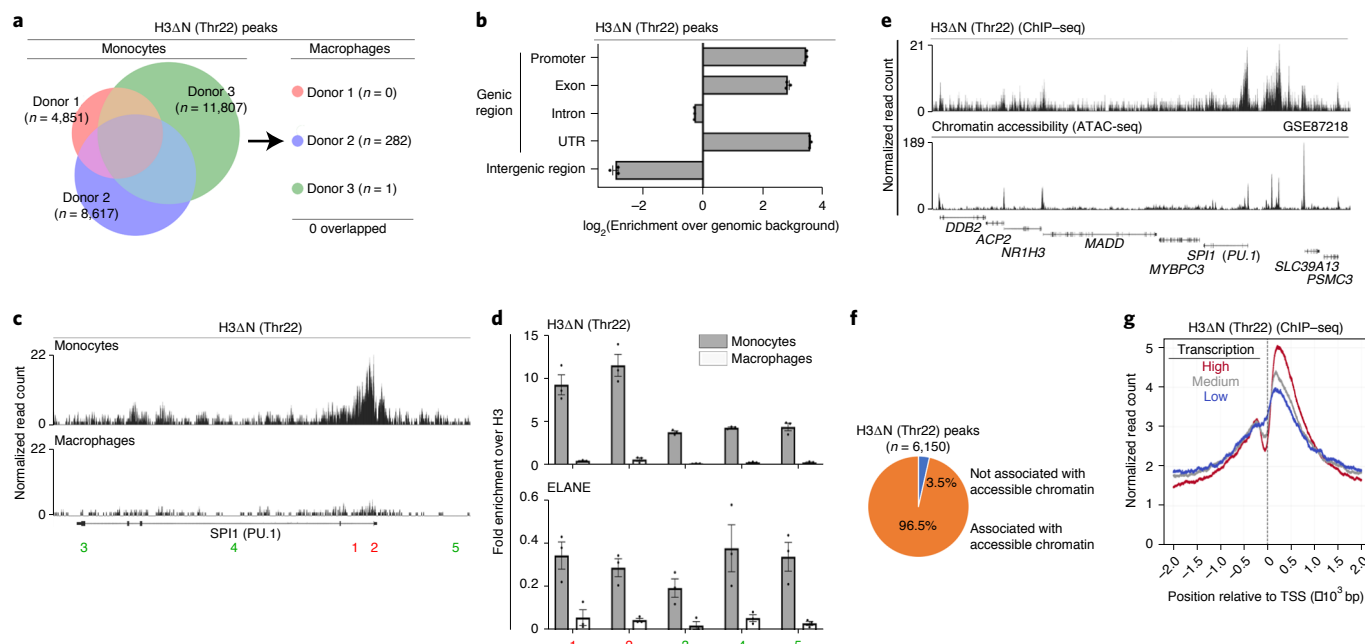
Fig. 5 | Permissive chromatin and active transcription association of H3ΔN in primary monocytes. a, Identification of H3ΔNThr22-enriched peaks in primary monocytes and paired monocyte-derived macrophages. Venn diagram depicts the number of H3ΔNThr22-enriched peaks in monocytes (left). The numbers of peaks identified in macrophages from the same donors are shown (right). **b,** Genic region enrichment of H3ΔNThr22 in primary monocytes. x axis, H3ΔNThr22 peak enrichment in the indicated genomic regions. Center line, genomic distribution with no enrichment. Data represent mean ± s.d. (three biological replicates). **c,d,** H3ΔNThr22 enrichment and ELANE occupancy at the PU.1 (SPI1) locus in primary monocytes. Representative genomic tracks of H3ΔNThr22 ChIP-seq data from primary monocytes (top) or macrophages (bottom) (**c**). Genomic regions with high (red) or low (green) H3ΔNThr22 ChIP-seq signals are tested. qPCR analysis of H3ΔNThr22 enrichment (top) or ELANE occupancy (bottom) in primary monocytes (gray) or in the matching monocyte-derived macrophages (white) using the indicated primer pairs. y axes, fold enrichment over bulk H3. Data represent mean ± s.e.m. (three technical replicates) (**d**). **e,f,** Association between H3ΔNThr22 enrichment and permissive chromatin at the peak level in primary monocytes. Representative genomic tracks of H3ΔNThr22 ChIP-seq (top) and ATAC-seq (GSE87218 (ref. [27])) (bottom) datasets from primary monocytes (**e**). Pie chart depicts the percentage of H3ΔNThr22 ChIP-seq peaks that are associated with ATAC-seq peaks (**f**). **g,** Association between H3ΔNThr22 enrichment and active transcription in primary monocytes. H3ΔNThr22 levels at the TSS-proximal regions for genes with high (red), medium (gray) or low (blue) transcription activities (GSE5099 (ref. [19])).

process (Fig. 7d, bottom). Together, these findings provide direct evidence that H3ΔN regulates gene expression reprogramming during cellular differentiation. NSP repression and the consequent H3ΔN depletion during monocyte-to-macrophage differentiation likely create a potentiated chromatin state that facilitates transcriptional alterations and promotes macrophage development.

Repressed H3ΔN in monocytes from patients with sJIA. We next investigated H3ΔN in sJIA, a pathologic condition where dysregulation of the monocyte and macrophage compartment has been implicated in disease pathophysiology[28,29]. We performed EpiTOF analysis of PBMCs from 16 patients with sJIA separated into two biological replicates with equivalent disease activity, in addition to ten age- and sex-matched healthy controls (HCs) (Fig. 8a and Supplementary Table 1). We measured the global levels of 40 histone marks in 16 major immune cell subtypes. Effect size comparison of the 640 parameters showed marked epigenetic alterations between HCs and patients with sJIA consistently captured in two independent biological replicates (Extended Data Fig. 8a) with negligible batch effect (Extended Data Fig. 8b). The epigenetic landscape between patients with sJIA and HCs was substantially distinct (Extended Data Fig. 8c). Monocyte-specific principal components analysis (PCA) separated patients with sJIA from HCs (Fig. 8b). H3ΔNThr22 in monocytes is lower in most patients with sJIA (Fig. 8c), with a median z-score 0.393 lower than that in HCs. However, significant heterogeneity was observed ($P = 2.3 \times 10^{-02}$, Bartlett's test on s.d.). Patients with sJIA receiving therapies targeting IL-1

(refs. [30,31]) (N = 5), or neutralizing TNF-α or on no biologic treatment (N = 6) showed lower H3ΔNThr22 in monocytes (Fig. 8d and Extended Data Fig. 8d). Patients treated with the IL-6 inhibitor tocilizumab[32] did not show reduced H3ΔNThr22 in monocytes. To validate these findings, we performed an expanded EpiTOF analysis on an independent cohort of 14 patients with sJIA and four HCs (Supplementary Table 2). Differential analysis found repressed H3ΔNThr22 in monocytes from patients with sJIA (Extended Data Fig. 8e). Notably, the only patient on tocilizumab therapy in this cohort showed the highest H3ΔNThr22 in monocytes among all patients, comparable to the HC level. Together, our data show reduced H3ΔNThr22 in sJIA-derived monocytes, suggesting that their chromatin state is primed for macrophage differentiation.

Ferritin-induced H3ΔNThr22 repression in monocytes. We next asked if soluble serum factors contribute to H3ΔNThr22 repression in monocytes from sJIA[28]. In vitro stimulation of PBMCs from 4 HCs treated ex vivo with sera from 14 patients with sJIA, 8 with active and 6 with quiescent disease (Supplementary Table 3) showed reduced H3ΔNThr22 in monocytes relative to cells treated with control sera (Fig. 8e). Moreover, sera from patients with sJIA with macrophage activation syndrome[33] induced a greater magnitude of H3ΔNThr22 reduction in HC monocytes (Fig. 8f and Extended Data Fig. 8f). The data argue that the dysregulated monocyte and macrophage compartment in patients with sJIA may be driven in part by signaling molecules present in the circulation. In vitro stimulations of HC monocytes
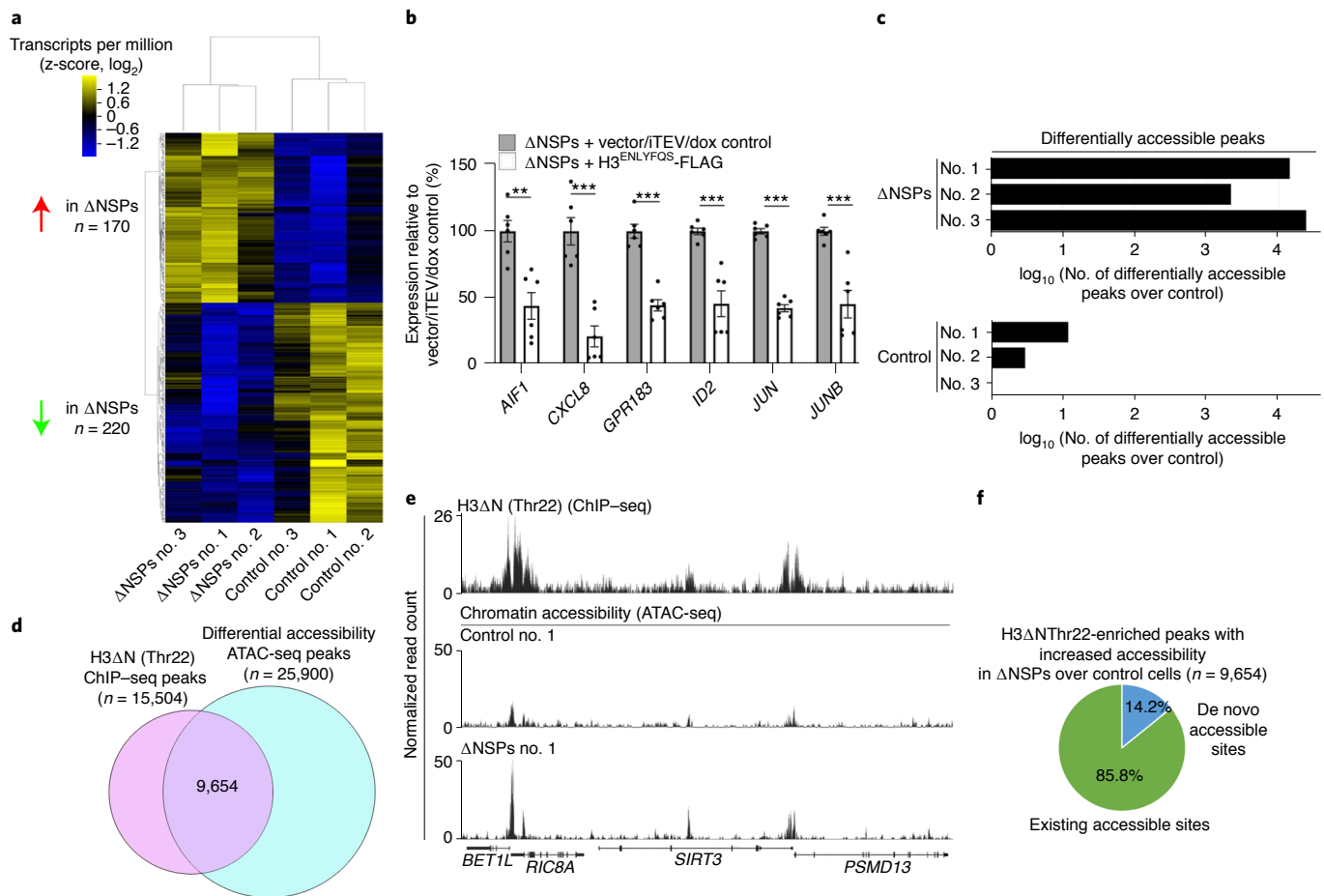
Fig. 6 | Global chromatin accessibility increase upon NSP and H3ΔNThr22 depletion. a, Differential gene expression in response to NSP depletion. Heatmap representation of differentially expressed genes between ΔNSPs and control cells under an FDR 5% cutoff. Z-score-transformed gene expression levels (color) of differential genes (*y* axis) in the indicated cell lines (*x* axis). Dendrogram, unsupervised clustering. **b**, Reintroducing H3ΔN into ΔNSPs cells attenuates the expression of genes upregulated in ΔNSPs cells. Gene expression analysis of ΔNSPs cells with (white) or without (gray) H3ΔN reintroduction as in Extended Data Fig. 2m. Data represent mean ± s.e.m. (three technical replicates and two biological replicates (independent ΔNSPs clones) (*N* = 6)). Statistical significance is determined by two-tailed Student's *t*-test. **P ≤ 0.01; ***P ≤ 0.001. **c**, Increased chromatin accessibility in ΔNSPs cells. ATAC-seq analysis of three controls and three ΔNSPs cell lines. The numbers of differentially accessible peaks are shown. Top, differentially accessible peaks in ΔNSPs clones over the average of controls; bottom, differentially accessible peaks in controls over the average of ΔNSPs clones. **d–f**, Increased chromatin accessibility at H3ΔNThr22-enriched peaks upon NSP and H3ΔNThr22 depletion. Venn diagram depicts the number of H3ΔNThr22 peaks identified in wild-type U937 cells associated with differentially accessible peaks between ΔNSPs and control cells (**d**). Representative genomic tracks of the H3ΔNThr22 ChIP–seq dataset from wild-type U937 cells (top) and ATAC-seq datasets from control (middle) or ΔNSPs (bottom) cells (**e**). Pie chart depicts the percentage of overlapped peaks in **d** (*N* = 9,654) that are existing accessible chromatin peaks in control cells (**f**).

with several cytokines and acute-phase reactants frequently elevated in sJIA sera[28] showed H3ΔNThr22 repression induced by IL-6 (Fig. 8g)[34]. In contrast, stimulations with IL-1β and IL-18 minimally impacted H3ΔNThr22 in monocytes (Extended Data Fig. 8g,h).

IL-6 blockade therapy reduces serum ferritin[35]. We found that ferritin purified from human liver induced H3ΔNThr22 repression in monocytes (Fig. 8h). To exclude the effects of possible contaminants carried over from primary human tissues, we validated the finding using ferritin purified from a recombinant source[36] (Fig. 8i and Extended Data Fig. 8i). Ferritin treatment in vitro suppressed NSP expression in HC monocytes (Fig. 8j) and promoted macrophage development (Fig. 8k). Together, our data support that both IL-6 and ferritin, two clinically important serum factors implicated in sJIA pathophysiology, may promote monocyte-to-macrophage differentiation through a chromatin-based mechanism involving regulated histone proteolysis.

Discussion

In this work, we identify a noncanonical nuclear function of NSPs in monocytes and their epigenetic role in governing cellular differentiation. An important open question is how NSPs are translocated to the nucleus in resting monocytes. Whether the same mechanisms controlling apoptosis or 'NETosis' are utilized but at an attenuated level, or there is a specialized transport system shuttling NSPs into the nuclei of resting monocytes requires further investigation.

NSPs share a similar promoter architecture[37]. During monocyte-to-macrophage differentiation, NSP repression likely involves *trans*-factors binding to the promoters of all three NSPs simultaneously. These regulators may be activated by signaling pathways that promote macrophage differentiation, such as macrophage colony-stimulating factor (M-CSF) and IL-6. Additionally, an open question is whether NSP and H3ΔN repression is specific to macrophage development or also occurs as monocyte
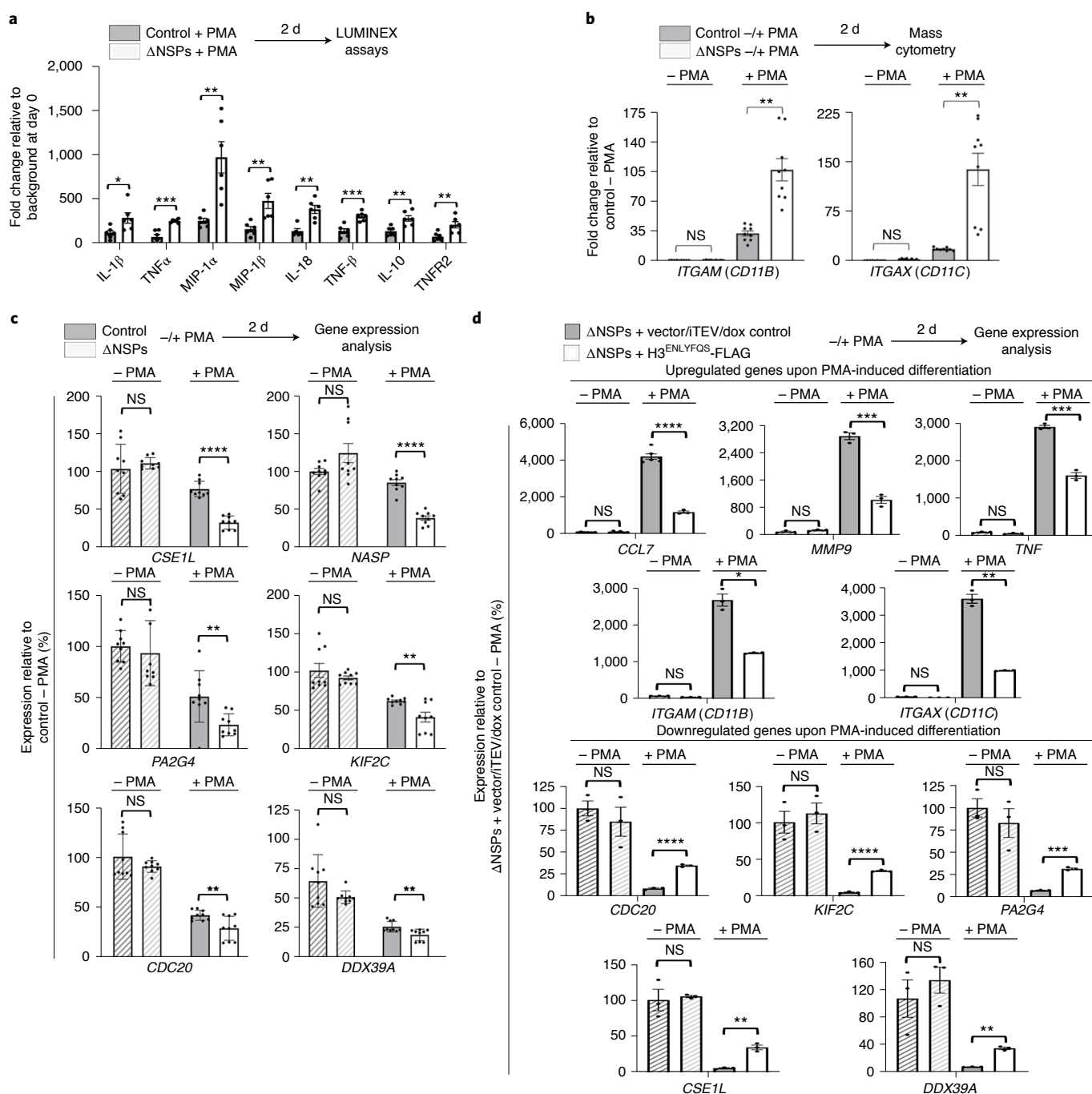
Fig. 7 | Chromatin priming mediated by NSP and H3ΔN repression facilitates gene expression reprogramming. a–c, ΔNSPs cells respond to PMA-induced differentiation with a greater magnitude of gene expression changes. Bead-based immunoassay analysis of the indicated cytokines. White, ΔNSPs cells; gray, control cells; y axis, fold change relative to the background at day 0 (**a**). Mass cytometry analysis of the cells as in **a** using antibodies targeting CD11b (left) or CD11c (right). y axis, fold change relative to the level in control cells without PMA stimulation (**b**). Gene expression analysis of the indicated genes. y axis, expression normalized against the level in control cells without PMA stimulation (**c**). Data represent mean ± s.e.m. (three (two in **a**) technical replicates from three ΔNSPs clones (white) or three control cell lines (gray) (N = 9 each). Statistical significance is determined by two-tailed Student's t-test. *P ≤ 0.05; **P ≤ 0.01; ***P ≤ 0.001; ****P ≤ 0.0001. **d**, Reintroducing H3ΔN into ΔNSPs cells attenuates cellular response to PMA-induced differentiation. Gene expression analysis of the cells as in Extended Data Fig. 2m treated with PMA to induce cellular differentiation. y axis, expression normalized against the level in control cells without PMA stimulation. Data represent mean ± s.e.m. (three technical replicates). Statistical significance is determined by two-tailed Student's t-test. *P ≤ 0.05; **P ≤ 0.01; ***P ≤ 0.001; ****P ≤ 0.0001. NS, not significant.

differentiation is skewed to dendritic cells. Cytokines that promote dendritic cell development, such as granulocyte–macrophage colony-stimulating factor (GM-CSF), IL-4 and TNF-α, may also regulate NSP expression.

The experiments where H3ΔN is reintroduced into ΔNSPs cells provide direct evidence that H3ΔN can induce chromatin architectural changes (Extended Data Fig. 2q) and affect cell morphology and functions (Extended Data Fig. 2n–p). However, future
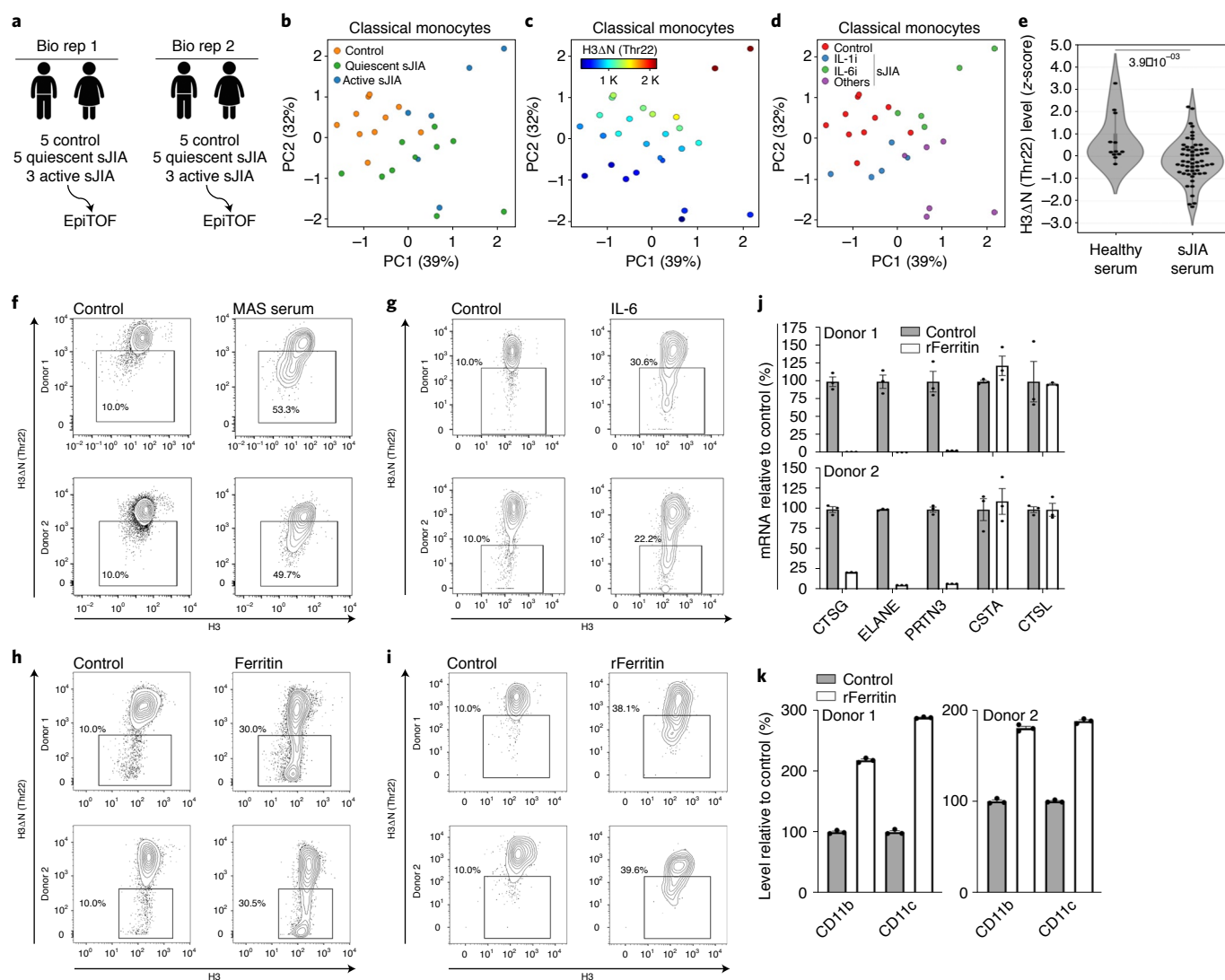
Fig. 8 | Repressed H3ΔN in patients with sJIA. a, EpiTOF analysis. **b**, Separation of monocytes from patients with sJIA or from healthy volunteers by histone modification profiles. PCA of EpiTOF data. Each dot, monocyte from a patient with sJIA; green, quiescent disease; blue, active disease; orange, healthy volunteer; %, the fraction of variance explained by each principal component. **c**, Reduced H3ΔN in monocytes from patients with sJIA. PCA as in **b**. Color, H3ΔNThr22 level. **d**, Patients with sJIA receiving IL-6 blockade therapy do not show reduced H3ΔNThr22 in monocytes. PCA as in **b**. Blue, biologics targeting IL-1 (IL-1i, canakinumab, anakinra or rilonacept); green, biologic targeting IL-6 (IL-6i, tocilizumab); purple, others (Results). **e**, Sera from patients with sJIA induce H3ΔN repression in monocytes from healthy volunteers. Mass cytometry analysis of H3ΔNThr22 levels in monocytes cultured in the presence of sera from 14 patients with sJIA (right, 56 data points) or 3 healthy donors (left, 12 data points) for 24 h. Statistical significance is determined by a mixed effect linear model with *P* value depicted. **f**, Sera from patients with sJIA with macrophage activation syndrome (MAS) induce marked H3ΔN reduction. Mass cytometry analysis of monocytes from two healthy donors (top and bottom) cultured in the presence of sera from a healthy donor (left) or a patient with sJIA with MAS (right) for 24 h. *x* axis, bulk H3 level; *y* axis, H3ΔNThr22 level. **g**, IL-6 induces H3ΔN reduction. In vitro stimulation assay as in **f** using IL-6. **h**, Native ferritin induces H3ΔNThr22 repression in monocytes. In vitro stimulation assay as in **f** using native ferritin. **i**, Recombinant ferritin (rFerritin) induces H3ΔNThr22 repression in monocytes. In vitro stimulation assay as in **f** using recombinant ferritin. **j**, Ferritin treatment suppresses NSP expression. qPCR analysis of the indicated genes (*x* axis). White, with recombinant ferritin; gray, without recombinant ferritin; *y* axis, expression relative to that in control cells; top, donor 1; bottom, donor 2. Data represent mean ± s.e.m. (three technical replicates). **k**, Ferritin promotes monocyte-to-macrophage differentiation. Mass cytometry analysis. White, with recombinant ferritin; gray, without recombinant ferritin. CD11b (left) and CD11c (right) expression is analyzed. Left, donor 1; right, donor 2; *y* axis, expression relative to control. Data represent mean ± s.e.m. (three technical replicates).

proteomic analysis will almost certainly find additional NSP substrates in the nucleus, whose involvements in transcription regulation and macrophage development require further investigation.

Asymmetric H3ΔN in monocytes is suggested in our work. First, H3ΔNThr22 ChIP using sheared chromatin containing predominantly mono-nucleosomes (Extended Data Fig. 4b) results in modest H3ΔN enrichment (Extended Data Fig. 4a). Second, the TSS-proximal H3ΔNThr22 enrichment at actively transcribed genes (Figs. 4h and 5g) is similar to that of H3K4me3 (ref. [38]). H3ΔNThr22 and H3K4me3 are mutually exclusive. However, both in U937 cells and in primary monocytes, we observe concurrent H3ΔNThr22 and H3K4me3 peaks using publicly available ChIP–seq datasets. Modification symmetry represents an important yet poorly understood aspect of chromatin regulation[39]. Future studies using sequential ChIP or nucleosome-resolution mass spectrometry[40] may provide additional insights into H3ΔN asymmetry.

Our data also raise an important question about how H3ΔN genomic distribution is determined in monocytes. First, NSP enzymatic activities may be modulated by MNEI/SERPINB1 (ref. [41]), whose nucleocytoplasmic distribution has been well-documented[42]. It is possible that a substantial proportion of ELANE molecules immunoprecipitated during our ChIP analysis are in complex with MNEI, which renders ELANE catalytically inactive. Second, crosstalk between H3ΔN and other histone modifications may affect its genomic distribution. NSP catalytic activities may be affected by pre-existing histone marks[43], and H3ΔN may promote or prevent subsequent modifications[44].

Our findings are of particular importance to the training and tolerance of innate immunity[45,46]. Several histone marks known to regulate innate immune memory, including H3K4me1, H3K4me3, H3K9me2, H3K27me3 and H3K27ac, are directly affected by H3ΔN. An integrative analysis of H3ΔN and these histone marks will allow us to better understand epigenetic regulation of innate immune memory.

EpiTOF analysis can be expanded to other diseases where monocytes and macrophages play key pathologic roles, such as atherosclerosis, hemophagocytic lymphohistiocytosis and other autoinflammatory conditions[47,48]. Our data link IL-6 to a chromatin-based mechanism promoting macrophage development[34]. IL-6 blockade is under clinical evaluation for giant cell arteritis, Takayasu arteritis and polymyalgia rheumatica. EpiTOF can be employed to investigate the relationships between H3ΔN in monocytes, tocilizumab therapy and disease activity in these vasculitides.

Identifying the receptor mediating ferritin uptake by monocytes[49,50] and characterizing the dependence of ferritin-induced chromatin alterations on its iron loading will provide important mechanistic insights. Elevated ferritin is found in sepsis and antiphospholipid syndrome, in which NSPs and H3ΔN may play key pathologic roles. Similarly, NSPs have been implicated in the pathophysiology of chronic obstructive pulmonary disease and acute lung injuries, for which targeting excessive NSP activities represents a promising therapeutic strategy[18]. Selective inhibition of pathologically relevant NSP functions will be key to the development of an efficacious and safe NSP inhibitor for therapeutic applications.

Online content

Any methods, additional references, Nature Research reporting summaries, source data, extended data, supplementary information, acknowledgements, peer review information; details of author contributions and competing interests; and statements of data and code availability are available at https://doi.org/10.1038/s41590-021-00928-y.

References

1. Dhaenens, M., Glibert, P., Meert, P., Vossaert, L. & Deforce, D. Histone proteolysis: a proposal for categorization into 'clipping' and 'degradation'. *Bioessays* **37**, 70–79 (2015).
2. Santos-Rosa, H. et al. Histone H3 tail clipping regulates gene expression. *Nat. Struct. Mol. Biol.* **16**, 17–22 (2009).
3. Xue, Y., Vashisht, A. A., Tan, Y., Su, T. & Wohlschlegel, J. A. PRB1 is required for clipping of the histone H3 N terminal tail in *Saccharomyces cerevisiae*. *PLoS ONE* **9**, e90496 (2014).
4. Duncan, E. M. et al. Cathepsin L proteolytically processes histone H3 during mouse embryonic stem cell differentiation. *Cell* **135**, 284–294 (2008).
5. Khalkhali-Ellis, Z., Goossens, W., Margaryan, N. V. & Hendrix, M. J. Cleavage of histone 3 by cathepsin D in the involuting mammary gland. *PLoS ONE* **9**, e103230 (2014).
6. Kim, K. et al. MMP-9 facilitates selective proteolysis of the histone H3 tail at genes necessary for proficient osteoclastogenesis. *Genes Dev.* **30**, 208–219 (2016).
7. Iwasaki, W. et al. Contribution of histone N-terminal tails to the structure and stability of nucleosomes. *FEBS Open Bio* **3**, 363–369 (2013).
8. Kouzarides, T. Chromatin modifications and their function. *Cell* **128**, 693–705 (2007).
9. Asp, P. et al. Genome-wide remodeling of the epigenetic landscape during myogenic differentiation. *Proc. Natl Acad. Sci. USA* **108**, E149–E158 (2011).
10. Fall, N. et al. Gene expression profiling of peripheral blood from patients with untreated new-onset systemic juvenile idiopathic arthritis reveals molecular heterogeneity that may predict macrophage activation syndrome. *Arthritis Rheum.* **56**, 3793–3804 (2007).
11. Ravelli, A. et al. 2016 classification criteria for macrophage activation syndrome complicating systemic juvenile idiopathic arthritis: a European League Against Rheumatism/American College of Rheumatology/Paediatric Rheumatology International Trials Organisation collaborative initiative. *Ann. Rheum. Dis.* **75**, 481–489 (2016).
12. Cheung, P. et al. Single-cell chromatin modification profiling reveals increased epigenetic variations with aging. *Cell* **173**, 1385–1397.e14 (2018).
13. Ziegler-Heitbrock, L. et al. Nomenclature of monocytes and dendritic cells in blood. *Blood* **116**, e74–e80 (2010).
14. Wilcox, D. & Mason, R. W. Inhibition of cysteine proteinases in lysosomes and whole cells. *Biochem. J.* **285**, 495–502 (1992).
15. Herrmann, C., Avgousti, D. C. & Weitzman, M. D. Differential salt fractionation of nuclei to analyze chromatin-associated proteins from cultured mammalian cells. *Bio Protoc.* **7**, e2175 (2017).
16. Luger, K., Rechsteiner, T. J. & Richmond, T. J. Preparation of nucleosome core particle from recombinant histones. *Methods Enzymol.* **304**, 3–19 (1999).
17. Hake, S. B. et al. Serine 31 phosphorylation of histone variant H3.3 is specific to regions bordering centromeres in metaphase chromosomes. *Proc. Natl Acad. Sci. USA* **102**, 6344–6349 (2005).
18. Korkmaz, B., Horwitz, M. S., Jenne, D. E. & Gauthier, F. Neutrophil elastase, proteinase 3, and cathepsin G as therapeutic targets in human diseases. *Pharm. Rev.* **62**, 726–759 (2010).
19. Martinez, F. O., Gordon, S., Locati, M. & Mantovani, A. Transcriptional profiling of the human monocyte-to-macrophage differentiation and polarization: new molecules and patterns of gene expression. *J. Immunol.* **177**, 7303–7311 (2006).
20. Holness, C. L. & Simmons, D. L. Molecular cloning of CD68, a human macrophage marker related to lysosomal glycoproteins. *Blood* **81**, 1607–1613 (1993).
21. Fabriek, B. O., Dijkstra, C. D. & van den Berg, T. K. The macrophage scavenger receptor CD163. *Immunobiology* **210**, 153–160 (2005).
22. Schulz, D., Severin, Y., Zanotelli, V. R. T. & Bodenmiller, B. In-depth characterization of monocyte-derived macrophages using a mass cytometry-based phagocytosis assay. *Sci. Rep.* **9**, 1925 (2019).
23. Mantovani, A., Sozzani, S., Locati, M., Allavena, P. & Sica, A. Macrophage polarization: tumor-associated macrophages as a paradigm for polarized M2 mononuclear phagocytes. *Trends Immunol.* **23**, 549–555 (2002).
24. Li, Q., Brown, J. B., Huang, H. & Bickel, P. J. Measuring reproducibility of high-throughput experiments. *Ann. Appl. Stat.* **5**, 1752–1779 (2011).
25. Haney, M. S. et al. Identification of phagocytosis regulators using magnetic genome-wide CRISPR screens. *Nat. Genet.* **50**, 1716–1727 (2018).
26. Zhang, Y. et al. Model-based analysis of ChIP-seq (MACS). *Genome Biol.* **9**, R137 (2008).
27. Novakovic, B. et al. β-Glucan reverses the epigenetic state of LPS-induced immunological tolerance. *Cell* **167**, 1354–1368.e14 (2016).
28. Mellins, E. D., Macaubas, C. & Grom, A. A. Pathogenesis of systemic juvenile idiopathic arthritis: some answers, more questions. *Nat. Rev. Rheumatol.* **7**, 416–426 (2011).
29. Schneider, R., Canny, S. P. & Mellins, E. D. in *Cytokine Storm Syndrome* (eds Cron, R. Q. & Behrens, E. M.) 349–379 (Springer International Publishing, 2019).
30. Ruperto, N. et al. Two randomized trials of canakinumab in systemic juvenile idiopathic arthritis. *N. Engl. J. Med.* **367**, 2396–2406 (2012).
31. Quartier, P. et al. A multicentre, randomised, double-blind, placebo-controlled trial with the interleukin-1 receptor antagonist anakinra in patients with systemic-onset juvenile idiopathic arthritis (ANAJIS trial). *Ann. Rheum. Dis.* **70**, 747–754 (2011).
32. De Benedetti, F. et al. Randomized trial of tocilizumab in systemic juvenile idiopathic arthritis. *N. Engl. J. Med.* **367**, 2385–2395 (2012).
33. Grom, A. A. & Mellins, E. D. Macrophage activation syndrome: advances towards understanding pathogenesis. *Curr. Opin. Rheumatol.* **22**, 561–566 (2010).
34. Chomarat, P., Banchereau, J., Davoust, J. & Palucka, A. K. IL-6 switches the differentiation of monocytes from dendritic cells to macrophages. *Nat. Immunol.* **1**, 510–514 (2000).
35. Schulert, G. S. et al. Effect of biologic therapy on clinical and laboratory features of macrophage activation syndrome associated with systemic juvenile idiopathic arthritis. *Arthritis Care Res. (Hoboken)* **70**, 409–419 (2018).

36. Santambrogio, P. et al. Production and characterization of recombinant heteropolymers of human ferritin H and L chains. *J. Biol. Chem.* **268**, 12744–12748 (1993).

37. Lennartsson, A., Garwicz, D., Lindmark, A. & Gullberg, U. The proximal promoter of the human cathepsin G gene conferring myeloid-specific expression includes C/EBP, c-myb and PU.1 binding sites. *Gene* **356**, 193–202 (2005).

38. Barski, A. et al. High-resolution profiling of histone methylations in the human genome. *Cell* **129**, 823–837 (2007).

39. Xie, J., Wooten, M., Tran, V. & Chen, X. Breaking symmetry—asymmetric histone inheritance in stem cells. *Trends Cell Biol.* **27**, 527–540 (2017).

40. Voigt, P. et al. Asymmetrically modified nucleosomes. *Cell* **151**, 181–193 (2012).

41. Cooley, J., Takayama, T. K., Shapiro, S. D., Schechter, N. M. & Remold-O'Donnell, E. The serpin MNEI inhibits elastase-like and chymotrypsin-like serine proteases through efficient reactions at two active sites. *Biochemistry* **40**, 15762–15770 (2001).

42. Bird, C. H. et al. Nucleocytoplasmic distribution of the ovalbumin serpin PI-9 requires a nonconventional nuclear import pathway and the export factor Crm1. *Mol. Cell Biol.* **21**, 5396–5407 (2001).

43. Simon, M. D. et al. The site-specific installation of methyl-lysine analogs into recombinant histones. *Cell* **128**, 1003–1012 (2007).

44. Schmitges, F. W. et al. Histone methylation by PRC2 is inhibited by active chromatin marks. *Mol. Cell* **42**, 330–341 (2011).

45. Netea, M. G. et al. Trained immunity: a program of innate immune memory in health and disease. *Science* **352**, aaf1098 (2016).

46. Saeed, S. et al. Epigenetic programming of monocyte-to-macrophage differentiation and trained innate immunity. *Science* **345**, 1251086 (2014).

47. Cheung, P., Khatri, P., Utz, P. J. & Kuo, A. J. Single-cell technologies—studying rheumatic diseases one cell at a time. *Nat. Rev. Rheumatol.* **15**, 340–354 (2019).

48. Cheung, P. et al. Single-cell epigenetics—chromatin modification atlas unveiled by mass cytometry. *Clin. Immunol.* **196**, 40–48 (2018).

49. Li, L. et al. Binding and uptake of H-ferritin are mediated by human transferrin receptor-1. *Proc. Natl Acad. Sci. USA* **107**, 3505–3510 (2010).

50. Chen, T. T. et al. TIM-2 is expressed on B cells and in liver and kidney and is a receptor for H-ferritin endocytosis. *J. Exp. Med.* **202**, 955–965 (2005).

51. McGuire, M. J., Lipsky, P. E. & Thiele, D. L. Generation of active myeloid and lymphoid granule serine proteases requires processing by the granule thiol protease dipeptidyl peptidase I. *J. Biol. Chem.* **268**, 2458–2467 (1993).

Methods

Cell culture and transfection. Jurkat, OCI-Lys3, U937 and THP-1 cells were cultured in RPMI 1640 media (Gibco) supplemented with 10% fetal bovine serum (FBS) (ATCC), glutamine (Gibco) and penicillin/streptomycin (Gibco) (referred to as complete media below unless otherwise specified). 293T cells were cultured in complete advanced DMEM media (ThermoFisher). Transfection of 293T cells with plasmid DNA was performed using TransIT-293 (Mirus) following the manufacturer's protocol.

Small-scale biochemical fractionation to isolate native chromatin. In total, 1×10^7 to 2×10^7 U937 cells, THP-1 cells or PBMCs were collected, washed with PBS and resuspended in buffer A (10 mM HEPES, pH 7.9, 10 mM KCl, 1.5 mM MgCl$_2$, 0.34 M sucrose, 10% glycerol, 1 mM dithiothreitol, complete protease inhibitor (Roche) and 1 mM PMSF)[52]. Triton X-100 was added to a final concentration of 0.1%. After incubating the cells for 8 min on ice, cells were centrifuged at 1,300g for 5 min at 4 °C. The supernatant containing the cytoplasm was clarified by centrifugation at 20,000g for 5 min at 4 °C. The nuclei were washed once with buffer A and lysed with buffer B (3 mM EDTA, 0.2 mM EGTA, 1 mM dithiothreitol, complete protease inhibitor and 1 mM PMSF) for 30 min. Chromatin was collected by centrifugation at 1,700g for 5 min at 4 °C. Chromatin was washed once with buffer B, resuspended in 5× SDS sample buffer (250 mM Tris-HCl pH 6.8, 10% SDS, 30% glycerol, 5% β-mercaptoethanol, 0.02% bromophenol blue), sonicated briefly to shear the DNA and boiled at 90 °C for 10 min before electrophoresis analysis.

Biochemical fractionation to isolate chromatin at different salt conditions. A total of 1×10^7 to 2×10^7 U937 cells were collected, washed with PBS and swelled in 5 packed cell volumes (PCV) of buffer A (10 mM Tris-HCl pH 7.9, 1.5 mM MgCl$_2$, 10 mM KCl, 1 mM PMSF, 0.5 mM dithiothreitol) for 10 min on ice. Cells were collected by centrifugation at 420g for 5 min and homogenized using a type B (loose) pestle in 2 PCV of buffer A. Nuclei were collected by centrifugation at 10,000g for 20 min, resuspended in 3 ml of buffer C (20 mM Tris-HCl pH 7.9, 0.42 M NaCl, 1.5 mM MgCl$_2$, 0.2 mM EDTA, 1 mM PMSF, 0.5 mM dithiothreitol, 25% glycerol) per 10^9 cells and homogenized using a type B pestle. The suspension was then gently rotated for 30 min at 4 °C. The nuclear extract was collected by centrifugation at 20,000g for 5 min. The chromatin pellet was washed with low-salt buffer (20 mM Tris-HCl pH 7.9, 1.5 mM MgCl$_2$, 0.2 mM EDTA, 0.15 M NaCl) three times. To extract NSPs from chromatin, chromatin was resuspended in high-salt buffer (20 mM Tris-HCl pH 7.9, 1.5 mM MgCl$_2$, 0.2 mM EDTA, 0.65 M NaCl).

Protein identification by mass spectrometry. To profile associated proteins in the purified chromatin fractions described above, the isolated native chromatin was subjected to mass spectrometry analysis (MSBioworks). Briefly, samples were loaded onto a 10% Bis-Tris SDS–PAGE gel (Novex, Invitrogen) and separated for approximately 1 cm. After Coomassie staining, the excised gel slice was washed with 25 mM ammonium bicarbonate followed by acetonitrile, reduced with 10 mM dithiothreitol at 60 °C followed by alkylation with 50 mM iodoacetamide at room temperature (RT) and digested with trypsin (Promega) at 37 °C for 4 h. The digested peptides were analyzed by nanoscale liquid chromatography coupled to tandem mass spectrometry (nano-LC-MS/MS) with a Waters NanoAcquity HPLC system interfaced to a ThermoFisher Q Exactive. Peptides were loaded on a trapping column and eluted over a 75-μm analytical column at 350 nl min⁻¹. Both columns were packed with Luna C18 resin (Phenomenex). The mass spectrometer was operated in data-dependent mode, with mass spectrometry and tandem mass spectrometry (MS/MS) performed in the Orbitrap at 70,000-full-width at half-maximum (FWHM) and 17,500-FWHM resolution, respectively. The 15 most abundant ions were selected for MS/MS. Data were searched using a local copy of Mascot and parsed into the Scaffold software for validation, filtering and to create a nonredundant list of identified proteins per sample.

CRISPR-mediated knock out strategy. Single guide RNAs (sgRNAs) targeting CTSL, CTSG, ELANE and PRTN3 were synthesized and cloned into plentiCRISPR v.2 to generate lentiviral particles for stable transduction. The sgRNA sequences are: 5′-ACTGGAAAGCATAATC CATT-3′ (CTSL no. 1); 5′-CAGTATGTTCAGGATA-3′ (CTSL no. 2); 5′-GGTCGTAGGAACCGAAGATG-3′ (CTSG no. 1); 5′-GATCTGAAGATACGCCATGT-3′ (CTSG no. 2); 5′-GGAAAAGACACGCGAGTCGG-3′ (ELANE no. 1); 5′- GAGTCGGCGGCCGAGGGTCA-3′ (ELANE no. 2); 5′-CACTTTCGTCCCTCGCCGCA-3′ (PRTN3 no. 1); and 5′-TGCTCGGAGCCCACAACGTG (PRTN3 no. 2). To generate a plasmid expressing sgRNA targeting CTSG, ELANE and PRTN3 simultaneously, oligos CTSG no. 2, ELANE no. 1 and PRTN no. 2 were cloned into pMule ENTR U6 stuffer sgRNA scaffold/plentiNeo using the multiple lentiviral expression (MuLE) system (Addgene). Transduced U937 cells were selected with 500 μg ml⁻¹ geneticin.

In vitro protease assay. First, 5 μg of recombinant cathepsin C (R&D systems) was incubated with 5 μg of recombinant ELANE (R&D systems) or PRTN3 (Novoprotein) for 2 h at 37 °C in PBS (Gibco) to activate these enzymes. Then, 10 μg of recombinant nucleosomes[16] were added and incubated for another

2 h at 37 °C. A sample with only cathepsin C was used as a control to exclude cleavage mediated by cathepsin C. For CTSG protease assay, 5 μg of recombinant CTSG (Sigma) was incubated with 10 μg of recombinant nucleosomes for 2 h at 37 °C. Reactions were terminated with 5× SDS sample buffer and run on a polyacrylamide gel followed by Coomassie staining. Excised gel slices were subjected to mass spectrometry analysis.

Mass spectrometry to identify H3 cleavage sites. Protein bands corresponding to cleaved H3 products were cut and digested with Glu-C endoproteinase in 50 mM NH$_4$HCO$_3$ buffer. Samples were reconstituted in 0.1% formic acid and analyzed on a Fusion Lumos mass spectrometer (Thermo Fisher Scientific) equipped with a Dionex Ultimate 3000 LC system. Peptides were separated by capillary reversed-phase chromatography on a 24-cm reversed-phase column (100 μm inner diameter, packed in-house with ReproSil-Pur C18-AQ 3.0 μm resin (Dr. Maisch GmbH)). Full mass spectrometry scans, data-dependent higher-energy collisional dissociation and EThcD (electron transfer dissociation with 25% of supplemental collision energy) MS/MS scans were all acquired in the Orbitrap mass analyzer. H3 cleavage products with cleavage sites ranging from H3K14 to H3R42 were analyzed. Peptide sequences were confirmed based on the EThcD spectra manually. In cases where multiple cleavage products were found, peak areas of the precursor peptides were used to compare the relative abundance of each cleavage product.

Cell sorting. FACS was performed as previously described[12]. Briefly, PBMCs were resuspended in PBS containing Zombie Aqua reagents (BioLegend) for 15 min at RT and quenched with mass cytometry (CyTOF) buffer (PBS, 1% BSA, 2 mM EDTA and 0.05% sodium azide). Cells were centrifuged at 400g for 8 min and resuspended in CyTOF buffer containing antibodies against immunophenotypic markers for 30 min. Markers for sorting: APC anti-CD19 (BioLegend) for B cells, PE-Cy7 anti-CD3 (BioLegend) for T cells, PE anti-CD14 (BioLegend) for monocytes and FITC anti-CD45 (BD) for total PBMCs. Cells were washed once in CyTOF buffer and twice in sorting buffer (PBS with 0.1% BSA). FACS was performed on sorters in the Stanford Shared FACS Facility. Sorted cells collected in CyTOF buffer were centrifuged at 400g for 8 min and resuspended in 5× SDS sample buffer at 1×10^6 cells per 100 μl. Samples were sonicated using Bioruptor (Diagenode) for 10 min before western blot analysis. To isolate clonal ΔNSPs U937 cells, single transduced cells were sorted into a 96-well plate filled with media based on forward and side scatters.

Reconstitution of H3ΔN in ΔNSPs U937 cells. Full-length H3 complementary DNA with TEV protease recognition site inserted between Ala21 and Thr22 and 3X-FLAG epitope tag was synthesized and cloned into pENTR3C (Invitrogen) and recombined into pLenti CMV Blast DEST (Addgene). TEV protease S219V mutant cDNA with added nuclear localization sequences was cloned into pCW57.1 (Addgene). For lentiviral transduction, viral particles were prepared with packaging plasmids pCMVΔ8.91 and pMD.G. Transduced ΔNSPs U937 cells were selected with 2 μg ml⁻¹ puromycin and 10 μg ml⁻¹ blasticidin. Cell lines were cultured in RPMI 1640 media (Gibco) supplemented with 10% FBS-TET tested (R&D Systems), glutamine (Gibco) and penicillin/streptomycin (Gibco). To induce the expression of TEV protease, cells were incubated with 5 μg ml⁻¹ doxycycline (Sigma) for 7 d.

In vitro cell migration assay. Control or ΔNSPs U937 cells were cultured in serum-free RPMI 1640 media overnight. Then, 1×10^6 cells were plated in the upper chamber of the 5-μm Transwell and incubated for 5 h. Lower chambers were filled with RPMI 1640 media with FBS. Cells were collected from the lower chamber, centrifuged at 300g for 5 min and resuspended in 100 μl of PBS for counting.

Phagocytosis assay. First, 1×10^5 cells were plated in 96-well plates and incubated with 18 μg of protein A Dynabeads (Invitrogen) for 4 h. The number of cells that contained the Dynabeads and the total number of cells were counted under the microscope. Each cell line was counted in three technical replicates. Phagocytosis of primary cells was measured using osmium-labeled *E. coli* and mass cytometry[22]. DH5-α *E. coli* was washed with PBS and fixed in 1.6% PFA (Electron Microscopy Sciences) for 10 min at RT at 1×10^9 cells per ml. Cells were washed twice with PBS and stained at a final concentration of 0.00008% OsO$_4$ for 7 min at RT. After staining, cells were washed twice with PBS, filtered and stored at −20 °C. For experiments, cytochalasin D was added to a concentration of 5 μM and incubated for 10 min. Unlabeled or osmium-labeled *E. coli* were added to primary cells at a 1:100 ratio and incubated for 30 min. Cells were then washed and processed for mass cytometry.

MNase sensitivity assay. First, 1×10^6 cells were centrifuged at 300g for 5 min and washed once with PBS. Cells were then treated with 1 ml of NP-40 buffer (10 mM Tris-HCl pH 7.4, 10 mM NaCl, 3 mM MgCl$_2$, 0.5% NP-40) and incubated on ice for 5 min. Nuclei were pelleted at 120g for 10 min and supernatant was removed by pipetting. MNase buffer (10 mM Tris-HCl pH 7.4, 15 mM NaCl, 60 mM KCl) was used to wash nuclei twice. Nuclei were resuspended in 200 μl of MNase buffer and treated with 0.015 U of MNase for 12 min at 37 °C. The reaction was

stopped with 100 μl of 0.5 M EDTA. Next, 3 μl of proteinase K and SDS to a final concentration of 2% were added and samples were incubated at 37 °C overnight. The next day, an equal volume of phenol/chloroform was added and samples were mixed and centrifuged at 16,000g for 10 min. The aqueous layer was pipetted off and transferred into a new tube. Samples were then incubated with 3 μl of RNase A at 37 °C for at least 2 h. An equal volume of chloroform was added and samples were mixed and centrifuged at 16,000g for 10 min. The aqueous layer was pipetted off and transferred into a new tube. A 1/7 volume of 3 M Na acetate and 2–2.5 volumes of ice-cold ethanol were added to each sample. Samples were incubated at −80 °C for at least 30 min. Samples were then centrifuged at 16,000g for 10 min at 4 °C. Supernatant was poured off, 1 ml of 70% ethanol was added and samples were centrifuged at 16,000g for 10 min. Ethanol was poured off and pellets were dried. DNA was resuspended in 50 μl of TE buffer at 55 °C and run on a 5% TBE gel.

Primary monocyte differentiation and macrophage polarization. Differentiation of monocytes to macrophages was performed following a standard protocol[19]. Mononuclear cells purified from buffy coat were plated and incubated overnight in complete RPMI 1640 media. The plates were washed three times with PBS (Gibco) to remove nonadherent cells, and the adherent cells were cultured for 7 d to allow for differentiation into macrophages. Alternatively, monocytes were isolated using the Pan Monocyte Isolation kit, a magnetic bead-based negative selection kit (Miltenyi Biotec, 130-096-537), and plated in RPMI media with 30 ng ml⁻¹ macrophage CSF. Plates were incubated for 5 d before collection of differentiated cells. To test the effects of NSP inhibition on differentiation, cells were cultured in media containing 100 μM AEBSF (Sigma) or 1 μM GW311616 hydrochloride ELANE inhibitor (APExBIO) and 1 μM CTSG inhibitor (APExBIO) for 2 d. To obtain polarized macrophages, monocyte-derived macrophages were first generated by the protocol described above. Naive macrophages were then cultured in media containing 100 ng ml⁻¹ LPS and 20 ng ml⁻¹ IFN-γ (classically activated) or 20 ng ml⁻¹ IL-4 (alternatively activated) for 18 h before collecting for western blot analysis.

Generation of U937 cells expressing exogenous NSPs. Full-length *CTSG*, *ELANE* or *PRTN3* cDNA was cloned into pENTR3C (Invitrogen)/pLenti CMV Blast DEST (Addgene) for overexpression in U937 cells. For lentiviral transduction, viral particles were prepared with packaging plasmids pCMVΔ8.91 and pMD.G. Transduced U937 cells were selected with 10 μg ml⁻¹ blasticidin. To induce differentiation of these transduced cells, cells were treated with 25 ng ml⁻¹ PMA for 1 d and cultured in complete media for 2 d. Cells were then collected for CyTOF and western blot analysis.

Cell preparation for ATAC-seq analysis. Three independently generated control cell lines and three ΔNSPs clones were pelleted, resuspended in fresh media with 1:100 volume of 100× DNase buffer (250 mM MgCl₂ and 50 mM CaCl₂) and 1:100 volume of DNase solution (20,000 units per ml of DNase in HBSS) (Invitrogen), and incubated at 37 °C for 30 min. Cells were then washed once with PBS and cryopreserved in media containing 5% DMSO before ATAC-seq analysis (Active Motif) following the standard protocol[53].

Transcriptomic profiling by RNA-seq. RNA was extracted from control and ΔNSPs U937 cells using the RNeasy Plus Mini Kit (Qiagen) following the manufacturer's protocol. Purified RNA was used for library construction and analyzed by high-throughput sequencing (Novogene).

ChIP–seq analysis. ChIP analysis was performed following a published protocol with minor changes[54]. Briefly, U937 cells were crosslinked with 1% formaldehyde (Sigma) for 8 min at RT with gentle mixing. The cross-linking reaction was stopped by adding a final concentration of 125 mM glycine and incubating for 5 min at RT. Cells were then centrifuged at 300g for 5 min and washed with PBS (Gibco) two times. Cells were resuspended in ChIP lysis buffer (50 mM HEPES-KOH pH 7.5, 140 mM NaCl, 1 mM EDTA pH 8.0, 1% Triton X-100, 0.1% sodium deoxycholate, 0.1% SDS and protease inhibitors) and incubated for 10 min on ice. Cell lysate was sonicated with Bioruptor (Diagenode) and diluted with RIPA buffer tenfold before incubating overnight with antibody/protein A magnetic bead complexes. Antibodies used were as follows: H3 (abcam, no. 1791), H3ΔNThr22 (Cell Signaling Technology, no. 12576), CTSG (abcam, no. 49854), ELANE (abcam 21595), PRTN3 (abcam, no. 133613). Beads were washed two times with ChIP wash buffer I (20 mM Tris pH 8.0, 0.1% SDS, 1% Triton, 0.1% sodium deoxycholate, 2 mM EDTA and 150 mM NaCl) and two times with ChIP wash buffer II (20 mM Tris-HCl pH 8.0, 0.1% SDS, 1% Triton, 0.1% sodium deoxycholate, 2 mM EDTA and 500 mM NaCl). Immunoprecipitated DNA was eluted from beads, de-crosslinked at 68 °C and purified using the MinElute PCR Purification Kit (Qiagen). Purified DNA was subjected to library preparation using the NEBNext Ultra II DNA Library Prep Kit (NEB) following the manufacturer's protocol. The DNA library was then submitted for sequencing at the Stanford Genome Sequencing Service Center.

Multiplex protein quantitation using the Luminex instrument platform. Control or ΔNSPs U937 cells were treated with 25 ng ml⁻¹ PMA for 1 d. Cells were washed with PBS and cultured in complete RPMI 1640 media for 2 d. Supernatant was collected, filtered through a 0.22-μM filter and stored at −80 °C for downstream

analysis. Multiplex protein quantitation was performed using the Human Immune Monitoring Panel of ProcartaPlex Multiplex Immunoassay (Invitrogen) following the manufacturer's protocol. In short, supernatant samples were diluted 1:10 and incubated with magnetic beads in a 384-well plate for 1 h at RT. Antibody/ streptavidin-PE conjugates were added for detection. Data were acquired using Luminex FlexMap 3D system (Luminex).

Mass cytometry sample processing, staining, barcoding and data acquisition. EpiTOF was performed following the protocol described previously[12]. Briefly, cryopreserved PBMCs were thawed and incubated in complete RPMI 1640 media at 37 °C for 1 h before processing. Cisplatin (ENZO Life Sciences) was added to 10 μM final concentration for 5 min before quenching with CyTOF buffer (PBS with 1% BSA, 2 mM EDTA and 0.05% sodium azide). Cells were centrifuged at 400g for 8 min and stained with lanthanide-labeled antibodies against immunophenotypic markers in CyTOF buffer containing Fc receptor blocker (BioLegend) for 30 min at RT. Following extracellular marker staining, cells were washed three times with CyTOF buffer and fixed in 1.6% PFA (Electron Microscopy Sciences) at 1×10⁶ cells per ml for 15 min at RT. Cells were centrifuged at 600g for 5 min and permeabilized with 1 ml of ice-cold methanol (Fisher Scientific) for 20 min at 4 °C. Then, 4 ml of CyTOF buffer was added to stop permeabilization followed by two PBS washes. Mass-tag sample barcoding was performed following the manufacturer's protocol (Fluidigm). Individual samples were then combined and stained with intracellular antibodies in CyTOF buffer containing Fc receptor blocker (BioLegend) overnight at 4 °C. The following day, cells were washed twice in CyTOF buffer and stained with 250 nM 191/193Ir DNA intercalator (Fluidigm) in PBS with 1.6% PFA for 30 min at RT. Cells were washed twice with CyTOF buffer and once with double-deionized water (ddH₂O) (ThermoFisher) followed by filtering through a 35-μm strainer. Cells were resuspended in ddH₂O containing four element calibration beads (Fluidigm) and analyzed by CyTOF (Fluidigm). Raw data were concatenated and normalized using calibration beads following the manufacturer's protocol for downstream processing.

PBMC isolation for in vitro stimulation assays. Mononuclear cells were purified from buffy coat by density gradient centrifugation using Ficoll-Paque Plus (GE Healthcare) in SepMate tubes (STEMCELL Technology). Crude PBMCs were treated with RBC lysis buffer (BioLegend) for 5 min to remove residual red blood cells followed by three PBS washes. Then, 2.5×10⁵ PBMCs were resuspended in 250 μl of RPMI with 20 μl of serum from healthy donors or patients with sJIA. Cells were processed for CyTOF analysis after overnight incubation. For in vitro PBMC stimulations, 1×10⁶ PBMCs were resuspended in 1 ml of RPMI and treated with 50 ng ml⁻¹ IL-6 (R&D), 25 ng ml⁻¹ IL-1B (R&D), 10 ng ml⁻¹ IL-18, 5 μg ml⁻¹ native ferritin (abcam) or 5 μg ml⁻¹ recombinant ferritin. All human subject research was approved by the Stanford Institutional Review Board.

Expression and purification of recombinant human ferritin. Full-length ferritin heavy chain and light chain cDNA was cloned into pET-21a (+) and pET-28a (+) vectors (Millipore), respectively. pET-21 ferritin heavy chain construct and pET-28 ferritin light chain construct were transformed into BL21-CodonPlus (DE3)-RILP Competent Cells (Agilent) sequentially. For protein expression, positive transformants were grown in LB medium with carbenicillin and kanamycin overnight. The saturated culture was diluted the following day to obtain an exponential-phase culture, to which 1.0 mM IPTG was added to induce ferritin expression for 2.5 h at 37 °C. Cells were pelleted and sonicated, and supernatant was heated at 70 °C for 15 min. Ferritin was isolated from the supernatant by centrifugation. Ferritin was purified by fast protein liquid chromatography using a HiPrep 26/60 Sephacryl S-300 HR gel filtration column (Sigma) filled with 50 mM Tris pH 7.5 and 50 mM NaCl buffer, followed by a HiTrap Q HP ion exchange column filled with 50 mM Tris pH 7.5 buffer with a 50–300-mM NaCl gradient. Purified protein was dialyzed to the buffer containing 50 mM Tris pH 7.5 and 50 mM NaCl for storage.

PCR primers.

Fig. 4d no. 1-F	tagcgctcttcttcggagtt
Fig. 4d no. 1-R	gggcggaaccaaacctaa
Fig. 4d no. 2-F	ggcgtccttcctaacatcc
Fig. 4d no. 2-R	tgtcaaatcacttgcccttg
Fig. 4d no. 3-F	gtcgggttccttcaaactca
Fig. 4d no. 3-R	gctcctgctggcttcttg
Fig. 4d no. 4-F	ttccacctcctggtttcaag
Fig. 4d no. 4-R	cgcttgtactcccagctacc
Fig. 4d no. 5-F	gcaggaaaatcgctggaa
Fig. 4d no. 5-R	cagtgctgccgtcttagctt
Fig. 4d no. 6-F	caattggcaggacagaacatc
Fig. 4d no. 6-R	gcataggcttgagggacaaa
Extended Data Fig. 4e no. 1-F	atacacagctacgggatacgg

Extended Data Fig. 4e no. 1-R	gctcggtttcaggagtttgt
Extended Data Fig. 4e no. 2-F	ccccttggaggaggacag
Extended Data Fig. 4e no. 2-R	cgaggaccctcgacttagaga
Extended Data Fig. 4e no. 3-F	ccaggctctgctgtctcg
Extended Data Fig. 4e no. 3-R	ggagacctcggctatcctg
Extended Data Fig. 4e no. 4-F	gctgtggctattatgacacataca
Extended Data Fig. 4e no. 4-R	tggatggttgactggaagg
Extended Data Fig. 4e no. 5-F	gcaggaggatcctttgaacc
Extended Data Fig. 4e no. 5-R	gaaacgagtttcattgtgttgc
Extended Data Fig. 4e no. 6-F	gagggatcccacctgacc
Extended Data Fig. 4e no. 6-R	cctggcctcacacctagact
Fig. 4l no. 1-F	caccctaccaggagacactca
Fig. 4l no. 1-R	ctccttgggccatcccta
Fig. 4l no. 2-F	gaggggaaacccttccatt
Fig. 4l no. 2-R	caggggatctgaccgactc
Fig. 4l no. 3-F	tctctcatttcctctctctaaacca
Fig. 4l no. 3-R	gactagggatgtgtgggtagga
Fig. 4l no. 4-F	ttttgatacaggcataaattgtgtaat
Fig. 4l no. 4-R	tgttggtaacacaaggaaatgaa
Fig. 4l no. 5-F	gtctgccctggctgagtg
Fig. 4l no. 5-R	gcagcagtggggtctttg
Extended Data Fig. 4m no. 1-F	tgagtcaaggttccctctgc
Extended Data Fig. 4m no. 1-R	tgactcagtttcccctctgg
Extended Data Fig. 4m no. 2-F	cggtgtggagggaaactg
Extended Data Fig. 4m no. 2-R	tggcccttgactcagcat
Extended Data Fig. 4m no. 3-F	ctctacaggggcttcgtgag
Extended Data Fig. 4m no. 3-R	catcttccctccctccact
Extended Data Fig. 4m no. 4-F	tgaaacgttagtcctttcaaataatc
Extended Data Fig. 4m no. 4-R	ccaaagcactggcattacaa
Extended Data Fig. 4m no. 5-F	tccctctgtttgcattgct
Extended Data Fig. 4m no. 5-R	agggaaggagaggtgaatgg
Extended Data Fig. 4m no. 6-F	gaaggtacagccactgtggaa
Extended Data Fig. 4m no. 6-R	ttgatcataggatagttccgtgttt
Extended Data Fig. 4m no. 7-F	ttctctgctttgttgtgttatgact
Extended Data Fig. 4m no. 7-R	cagagtggcacttgtctgtga
CSE1L-F	agattctgctaacaaaccttttcaa
CSE1L-R	ggagagaaaaacttctcatgatagc
NASP-F	cagatgaaagaggtgaagaaac
NASP-R	tttggcatttcttcggtctta
PA2G4-F	cagggcctggcttaggag
PA2G4-R	cagactctagccgctctcg
KIF2C-F	ccctcagttgtcgccctca
KIF2C-R	ggaaagaagggcaacacaaa
CDC20-F	ctgtctgagtgccgtggat
CDC20-R	tccttgtaatggggagacca
DDX39A-F	ggtttgaagttaatgtggcagaa
DDX39A-R	gttaccggctctgctcgat
CCL7-F	atgaagcacctggacaagaaa
CCL7-R	gaaccactctgagaaaggacag
MMP9-F	gaactttgacagcgacaagaag
MMP9-R	cggcactgaggaatgatctaa
TNF-F	agagggagagaagcaactaca
TNF-R	gggtcagtatgtgagaggaaga
ITGAM-F	tcagcatcaccttcagtttca
ITGAM-R	ggagtcctcaccatcatttctc
ITGAX-F	actcagatcggctcctactt
ITGAX-R	gttagcagccacgaacaattc

Computational methods. *RNA-seq analysis.* FASTQ files were assessed for quality using FastQC[55] (available online at: http://www.bioinformatics.babraham.ac.uk/projects/fastqc) and aligned to the human genome (GRCh38 assembly) using HISAT2 (ref. [56]). Following alignment, HTSeq-counts[57] was used to produce gene-level counts (using gene features from ENSEMBL) which were supplied to DESeq2 (ref. [58]) to determine differentially expressed genes between control U937 cells and ΔNSPs U937 cells at an FDR cutoff of 5%. To account for transduction batch effects, transduction batch was included as a covariate in the DESeq2 analysis. DAVID[59] was used to determine enriched gene ontology terms using the list of differentially expressed genes. To generate the heatmap of differentially expressed genes, genes where all counts were 0 were removed and log2-transformed transcripts per million were calculated for the remaining genes. A linear model including a covariate for transduction batch was then used to correct for batch effects. Genes were then filtered, keeping genes with FDR < 5% (as determined by DESeq2), and then plotted using Seaborn Clustermap[60]. Samples and genes were clustered using hierarchical clustering with the Euclidean distance metric and Ward's minimum variance method for linkage. The values plotted are z-score transformed across each gene.

ATAC-seq analysis. FASTQ files for the ATAC-seq datasets were analyzed using PEPATAC (http://code.databio.org/PEPATAC/) with parameters as described by Corces et al.[61] The control U937 cell line was used as the control/background population for MACS2 (ref. [26]). Briefly, adapters were trimmed using Skewer[62], followed by removal of reads aligning to the Revised Cambridge Reference Sequence of human mitochondrial DNA (http://www.ncbi.nlm.nih.gov/nuccore/251831106) and human repeats (https://github.com/databio/ref_decoy) references. The resulting reads were then aligned to the human genome (GRCh38) using bowtie2 (ref. [63]) and duplicates were removed using Picard Tools (https://broadinstitute.github.io/picard/). MACS2 callpeak was then used to discover peaks in the pooled ΔNSPs reads with a comparison with the pooled control U937 cell line alignments as background (or discovering peaks in pooled control U937 without a background for comparison) at a Q value of 5%, using options 'nomodel' and 'keep-dup all'.

As described by Corces et al.[61], peak summits were extended by 250 bp in both directions and removed if they extended beyond the chromosome ends or if they were within blacklisted regions from the ENCODE project[64]. To assess the quality of the data, read counts per million at each base in a range of −1,000 to +1,000 from all annotated TSSs were plotted. Peaks were classified as being in promoters, exons, introns, UTRs or intergenic regions by determining if the peak overlapped with a UTR ('five_prime_utr' or 'three_prime_utr'), exon or intron (peak within a gene but not in a promoter, exon or UTR), as annotated by Ensembl (https://uswest.ensembl.org/info/data/ftp/index.html). As promoters are not annotated, a window of 2,000 bp was used from the TSS. All other peaks were classified as intergenic. The fraction of peaks in each of these features was then compared with the genomic background, that is, the expected distribution if the peaks were uniformly distributed. Enrichment statistics were calculated using the normal approximation of the hypergeometric distribution for large N. The number of reads across selected genes (as determined by the Luminex cytokine assay) was calculated as pileups generated by 'samtools mpileup' and then plotted.

ChIP–seq analysis. PEPATAC was used to perform the alignment and preprocessing of the FASTQ files from three biological replicates for ChIP–seq for both macrophages and monocytes. The resulting aligned, sorted and deduplicated BAM files were then supplied to MACS2 using a Q value of 5% to call peaks with a comparison against H3. Peaks were annotated by genomic feature as described for ATAC-seq data. Few peaks were found in macrophages and they did not overlap across biological replicates. To select consistent peaks for the monocytes, peaks were first merged across the three biological replicates (that is, if any part of a peak overlapped with any part of another, no matter which replicate it came from, the peaks were merged into a single peak). Peaks with at least two biological replicates represented were used for downstream analysis. Normalized pileups for each gene were plotted with ATAC-seq pileups. The same analysis was then completed for all TSSs to plot normalized reads relative to TSSs.

To compare H3ΔNThr22 ChIP–seq with the monocyte transcriptional profile from GSE5099, mean expression from that dataset was used to bin genes into low-, medium- and highly expressed genes by taking the first, second and third terciles, respectively. ChIP–seq signals (pileups) were calculated for TSSs for genes in these groups with a bandwidth of 4 kb. The aggregate signal across the three biological replicates was included in the plot.

For U937 cells, two biological replicates were processed using PEPATAC and MACS2 as described above (with a lenient Q value of 25% as recommended for the following filtering steps). The resulting peaks from the two biological replicates were sorted and then filtered using the IDR method (https://github.com/nboley/idr), ranking by signal value. The IDR cutoff of 5% was then used to filter for significant peaks.

To compare H3ΔNThr22 ChIP–seq in U937 cells with the U937 transcriptional profile from GSE107566, mean expression from that dataset was used to bin genes into low-, medium- and highly expressed genes by taking the first, second and third terciles, respectively. ChIP–seq signals (pileups) were calculated for TSSs for genes in these groups with a bandwidth of 4 kb. The aggregate signal across the three biological replicates was included in the plot.

ATAC-seq versus ChIP-seq analysis. To calculate the cross-correlation between ATAC-seq and U937 H3ΔNThr22 ChIP-seq data, a representative bigwig file generated by PEPATAC for both the ATAC-seq and ChIP-seq data was processed by the numpy (v.1.18.1) 'correlate' function over a region of 10 kb from a randomly selected starting nucleotide. The correlations were then normalized analogously to Pearson correlation by dividing the raw correlation values by the square root of the product of each signal taken as a dot product with itself. This process was completed 1,000 times and the results averaged for each shift/offset.

To find H3ΔNThr22 ChIP-seq peaks overlapping with ATAC-seq peaks, in both U937 cells and primary monocytes, ATAC-seq peaks found in ΔNSPs U937 cells and not U937 controls were first merged and compared with H3ΔNThr22 ChIP-seq peaks. Any portion of a peak overlapping another was counted as an overlap.

EpiTOF analysis. For both experiments involving EpiTOF (PBMCs derived from patients with sJIA and healthy PBMCs exposed to sJIA sera), CSV files representing hand-gated populations of monocytes were exported from FlowJo and preprocessed as described previously[12]. To summarize, histone modification marker levels were normalized to total H3/H4 by fitting a linear model with H3 and H4 values as covariates and the marker as the response variable. The residuals were then used for downstream analyses. Cell population-level means for each marker were then calculated and used in PCA. The sample correlation matrix rather than the sample covariance matrix was used for each PCA.

Statistics and reproducibility. Statistical analysis for nonsequencing data was performed using GraphPad Prism software. Unpaired two-tailed Student's *t*-test was used unless otherwise stated. *$P < 0.05$; **$P < 0.01$; ***$P < 0.001$; ****$P < 0.0001$. For the EpiTOF analyses related to sJIA samples, a preliminary unpublished dataset on H3ΔThr22 levels in patients with sJIA suggested marked decrease in H3ΔThr22 level in sJIA relative to that in healthy subjects with effect sizes < -1. Using this estimate, a power analysis assuming an unpaired one-tailed *t*-test at 80% power, effect size -1 and significance level 0.05 was performed. The analysis suggested that a sample size greater than 13 is required. We were able to obtain clinical samples from 16 patients with sJIA. Samples from patients with quiescent or active sJIA were randomly assigned and analyzed in two biological replicates. Samples from healthy volunteers were obtained from Stanford Blood Center with age being the only selection criterion (between 17 and 18). All samples were randomly assigned to different experimental groups. For analyses related to the sJIA serum, no statistical method was used to predetermine sample size. The design was based on the number of samples that can be barcoded for combined mass cytometry processing and analysis to minimize technical variability. All experiments described in the manuscript were repeated at least two times. Statistical analyses for sequencing data are described above. No statistical method was used to predetermine sample size. For ChIP-seq, we analyzed wild-type U937 cells in two biological replicates. ChIP-seq analysis of H3ΔThr22 was performed on three primary monocyte samples and their matching monocyte-derived macrophages. ATAC-seq and RNA-seq were employed to analyze three ΔNSPs clones and control cell lines. The sequencing experiments were not randomized. For all analyses, no data were excluded. The investigators were not blinded to allocation during experiments and outcome assessment. All replicates were successful. All measurements were objectively quantifiable (for example, instrument output). Thus, blinding was not applicable.

Reporting Summary. Further information on research design is available in the Nature Research Reporting Summary linked to this article.

Data availability

ChIP-seq, ATAC-seq and RNA-seq datasets have been deposited in the Gene Expression Omnibus (GEO) with accession numbers GSE142661, GSE142660 and GSE142662, respectively. Other data generated and/or analyzed during the current study and all reagents, including cell lines and plasmid DNA, described in this work are available from the corresponding author on reasonable request. Figures associated with individual datasets are listed as follows: ATAC-seq, GSE142660 (Figs. 4e–g and 6c–f and Extended Data Figs. 4g, 6a,c,d,e and 7a–c); ChIP-seq, GSE142661 (Figs. 4a–c,e–h, 5a–c,e–g and 6d–f and Extended Data Figs. 4c,d,g, 5c–f and 6e); RNA-seq, GSE142662 (Fig. 6a and Extended Data Fig. 6a,b). Source data are provided with this paper.

Code availability

Custom code and mathematical algorithms to analyze ChIP-seq, ATAC-seq, RNA-seq and EpiTOF datasets are available from the corresponding author on reasonable request.

References

52. Mendez, J. & Stillman, B. Chromatin association of human origin recognition complex, Cdc6, and minichromosome maintenance proteins during the cell cycle: assembly of prereplication complexes in late mitosis. *Mol. Cell Biol.* **20**, 8602–8612 (2000).
53. Buenrostro, J. D., Wu, B., Chang, H. Y. & Greenleaf, W. J. ATAC-seq: a method for assaying chromatin accessibility genome-wide. *Curr. Protoc. Mol. Biol.* **109**, 21.29.21–21.29.29 (2015).
54. Dahl, J. A. & Collas, P. Q2ChIP, a quick and quantitative chromatin immunoprecipitation assay, unravels epigenetic dynamics of developmentally regulated genes in human carcinoma cells. *Stem Cells* **25**, 1037–1046 (2007).
55. Andrews, S. *FastQC: A Quality Control Tool for High Throughput Sequence Data* (Babraham Bioinformatics, Babraham Institute, 2010).
56. Kim, D., Langmead, B. & Salzberg, S. L. HISAT: a fast spliced aligner with low memory requirements. *Nat. Methods* **12**, 357–360 (2015).
57. Anders, S., Pyl, P. T. & Huber, W. HTSeq—a Python framework to work with high-throughput sequencing data. *Bioinformatics* **31**, 166–169 (2015).
58. Love, M. I., Huber, W. & Anders, S. Moderated estimation of fold change and dispersion for RNA-seq data with DESeq2. *Genome Biol.* **15**, 550 (2014).
59. Huang, D. W., Sherman, B. T. & Lempicki, R. A. Systematic and integrative analysis of large gene lists using DAVID bioinformatics resources. *Nat. Protoc.* **4**, 44–57 (2009).
60. Waskom, M. et al. mwaskom/seaborn v.0.9.0 (Zenodo, 2018); https://doi.org/10.5281/zenodo1313201
61. Corces, M.R. et al. The chromatin accessibility landscape of primary human cancers. *Science* **362**, eaav1898 (2018).
62. Jiang, H., Lei, R., Ding, S. W. & Zhu, S. Skewer: a fast and accurate adapter trimmer for next-generation sequencing paired-end reads. *BMC Bioinf.* **15**, 182 (2014).
63. Langmead, B. & Salzberg, S. L. Fast gapped-read alignment with Bowtie 2. *Nat. Methods* **9**, 357–359 (2012).
64. The ENCODE Project Consortium. An integrated encyclopedia of DNA elements in the human genome. *Nature* **489**, 57–74 (2012).

Author contributions

P.C., S.S. and A.J.K. conceived the molecular biology, cell biology and biochemistry experiments. P.C., S.E.C. and M. Dvorak performed experiments with assistance from M.H.F. S.S. performed computational analyses of EpiTOF, ChIP-seq, ATAC-seq and RNA-seq data with assistance from M. Donato. P.C. and A.J.K. interpreted the data with help from S.S. C.M. coordinated sJIA clinical sample selection and compiled clinical information. T.-M.L. performed mass spectrometry analysis to identify proteolytic cleavage sites with assistance from L.Z., J.P.C. and J.E.E. under the supervision of O.G. G.S.S., A.A.G., L.A.H. and P.A.N. collected sJIA samples and associated clinical data. E.D.M. provided input on experimental strategies, monocyte biology and sJIA pathophysiology and sJIA samples with associated clinical data. P.K. supervised the computational analyses. P.J.U. supervised the work conducted in the experimental laboratory. P.C. and A.J.K. wrote the manuscript with contributions from all coauthors. All authors discussed and commented on the manuscript.

Extended Data Fig. 1 | See next page for caption.

Extended Data Fig. 1 | CTSG, ELANE, and PRTN3-Mediated H3ΔN in Monocytes. a, H3ΔNThr22 enrichment in monocytes is not associated with cell death. Viability of the cells shown in Fig. 1a measured by cisplatin staining. Data represent mean ± S.E.M. (N = 20). **b**, CD14⁺CD16⁻ classical monocyte-specific H3ΔNThr22 enrichment. EpiTOF analysis of the indicated monocyte subsets. Y-axis, normalized H3ΔNThr22 level; center line, median; box limits, upper and lower quartiles; whiskers, 1.5x interquartile range; points, outliers. Statistical significance is determined by two-tailed Welch's *t*-test with *P* values depicted. **c**, Inverse relationship between class II MHC expression and H3ΔNThr22 in monocytes. Single-cell analysis of EpiTOF data as in (**a**). Each dot represents a single monocyte. X-axis, HLA-DR; y-axis, H3ΔNThr22 (top) or bulk H3 levels (bottom). **d**, Chromatin localization of H3ΔN in monocytic cells. Western blot analysis of THP-1 cells biochemically separated into cytoplasmic and insoluble chromatin fractions. **e**, H3ΔN in monocytes is not catalyzed by cathepsin L. Western blot analysis of WCE from THP-1 cells expressing CRISPR-Cas9 and two independent sgRNAs targeting *CTSL*. Control cells express CRISPR-Cas9 but lack sgRNA. **f**, H3ΔN in monocytes is not catalyzed by matrix metalloproteases (MMPs). Western blot analysis of WCE from U937 (top) or THP-1 (bottom) cells treated with MMP9-specific or broad-spectrum MMP inhibitors. Control, DMSO treated. **g**, H3ΔN in monocytes is not catalyzed by cysteine proteases. Western blot analysis of WCE from U937 (left) or THP-1 (right) cells cultured in the presence of a cell-permeable broad-spectrum cysteine protease inhibitor E-64d. Control, DMSO treated. **h**, Serine proteases generate H3ΔN in monocytic THP-1 cells. Western blot analysis of WCE from THP-1 cells treated with nonselective serine protease inhibitor AEBSF. Control, PBS treated. **i**, Chromatin localization of CTSG, ELANE, and PRTN3. Western blot analysis of the cytoplasmic and chromatin-enriched fractions purified from THP-1 cells. **j**, Release of chromatin-bound NSPs in high-salt solution. Chromatin pellet as in Fig. 1d is washed extensively with a buffer containing physiological ionic strength and is subsequently treated with a high-salt solution to solubilize chromatin proteins. Supernatant (left) and pellet (right) fractions are subject to immunoblotting analysis. HP1α serves as a chromatin protein control. **k**, Controlled proteolytic activities of CTSG, ELANE, and PRTN3 on nucleosomal H3 *in vitro*. Tandem mass spectrometry analysis of protease assays as in Fig. 1h using individual NSPs and recombinant nucleosomes. Primary cleavage sites accounting for greater than 20% of proteolytic products are labeled. CTSG (red); ELANE (green); PRTN3 (blue). **l,m**, Distinct histone modification profiles between FL- and truncated H3. Immunoblotting analysis of WCE from U937 cells (**l**) or primary monocytes (**m**) using the indicated antibodies. Three biological replicates are shown. These results are used for the quantitative analyses shown in Figs. 1i and 1j.
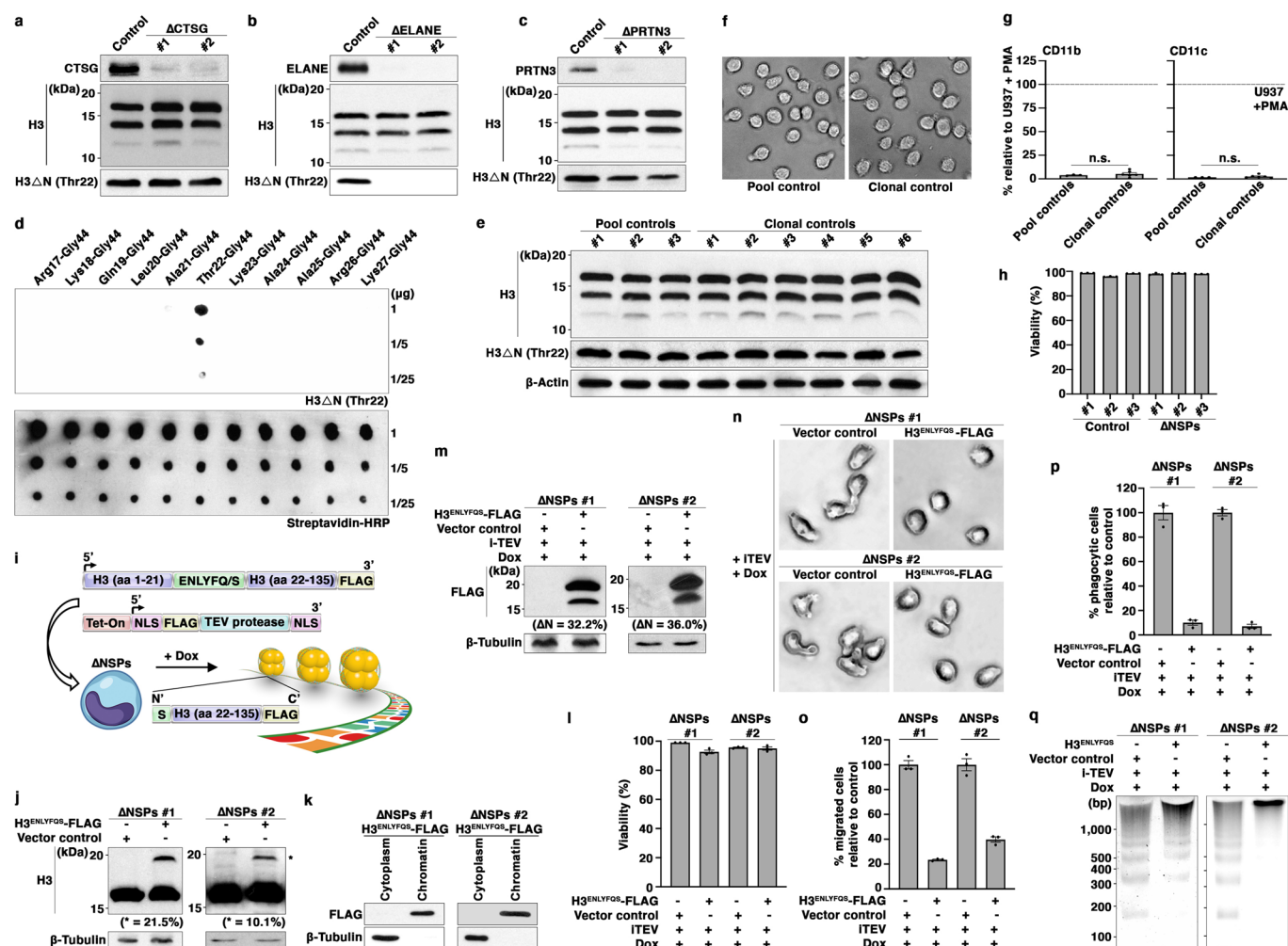
Extended Data Fig. 2 | Reintroduction of H3ΔN into ΔNSPs Cells Reverses the Morphologic and Functional Alterations Associated with NSP Depletion.
a, **b**, **c**, Depletion of individual NSPs does not affect global H3ΔN level in monocytes. Western blot analysis of WCE from U937 cells depleted of CTSG
(**a**), ELANE (**b**), or PRTN3 (**c**). Control cells express CRISPR-Cas9 but lack sgRNA. **d**, Highly specific anti-H3ΔNThr22 antibody used in this study.
Dot blot analysis of the anti-H3ΔNThr22 antibody using the indicated synthetic peptides. This affinity reagent is employed throughout the entire study.
e, **f**, **g**, Clonal selection by FACS does not alter H3ΔN level and pattern, cell morphology, or activation markers CD11b and CD11c expression. Western
analysis of WCE from control cells as in Fig. 2a with (six samples on the right) or without (three samples on the left) clonal selection by FACS **e**,
Representative light microscopy images of the control cells as in (**e**) (**f**). Mass cytometry analysis of the cells as in (**e**) (**g**). Y-axis, mean signal intensities
of CD11b (left) or CD11c (right) from the indicated cells relative to the signals from PMA-activated U937 cells as a positive control. Data represent
mean ± S.E.M. (three pool controls (left) or six clonal controls (right)). Clonal controls are randomly selected from approximately 400 sorted clones.
Statistical significance is determined by two-tailed Student's t-test. **h**, Simultaneous NSP depletion does not affect cell viability. Mass cytometry analysis
of ΔNSPs and control cells. The percentage of cells negative for cisplatin staining for each cell line is shown. Data represent mean ± S.E.M. (three technical
replicates). **i**, Strategy to reintroduce H3ΔN into ΔNSPs cells. **j**, Expression of epitope-tagged exogenous H3 (H3^{ENLYFQS}-FLAG) in ΔNSPs cells. Western blot
analysis of WCE from ΔNSPs cells transduced with H3^{ENLYFQS}-FLAG (right lane) or empty vector (left lane). The relative abundance of H3^{ENLYFQS}-FLAG to
endogenous H3 determined by ImageJ software is shown. **k**, Chromatin localization of exogenous H3. Western blot analysis of cytoplasmic and chromatin
fractions from ΔNSPs cells expressing H3^{ENLYFQS}-FLAG. **l**, Doxycycline treatment to induce TEV protease expression and H3^{ENLYFQS}-FLAG cleavage does
not affect cell viability. Viability of the indicated cells is determined by trypan blue staining and an automatic cell counter. Data represent mean ± S.E.M.
(three technical replicates). **m**, H3^{ENLYFQS}-FLAG cleavage in response to doxycycline-induced TEV protease expression. Western analysis of WCE from the
indicated cells. The abundance of cleavage product relative to total H3^{ENLYFQS}-FLAG is determined by ImageJ software. **n**, **o**, **p**, Reintroduction of H3ΔN
into ΔNSPs cells reverses morphological and functional alterations associated with NSP depletion. Light microscopy (**n**), transwell cell migration (**o**), and
phagocytosis (**p**) analyses of the cells as in (**m**). Data represent mean ± S.E.M. (three technical replicates). **q**, Reintroduction of H3ΔN into ΔNSPs cells
alters global chromatin architecture. MNase sensitivity analysis of the cells as in (**m**).
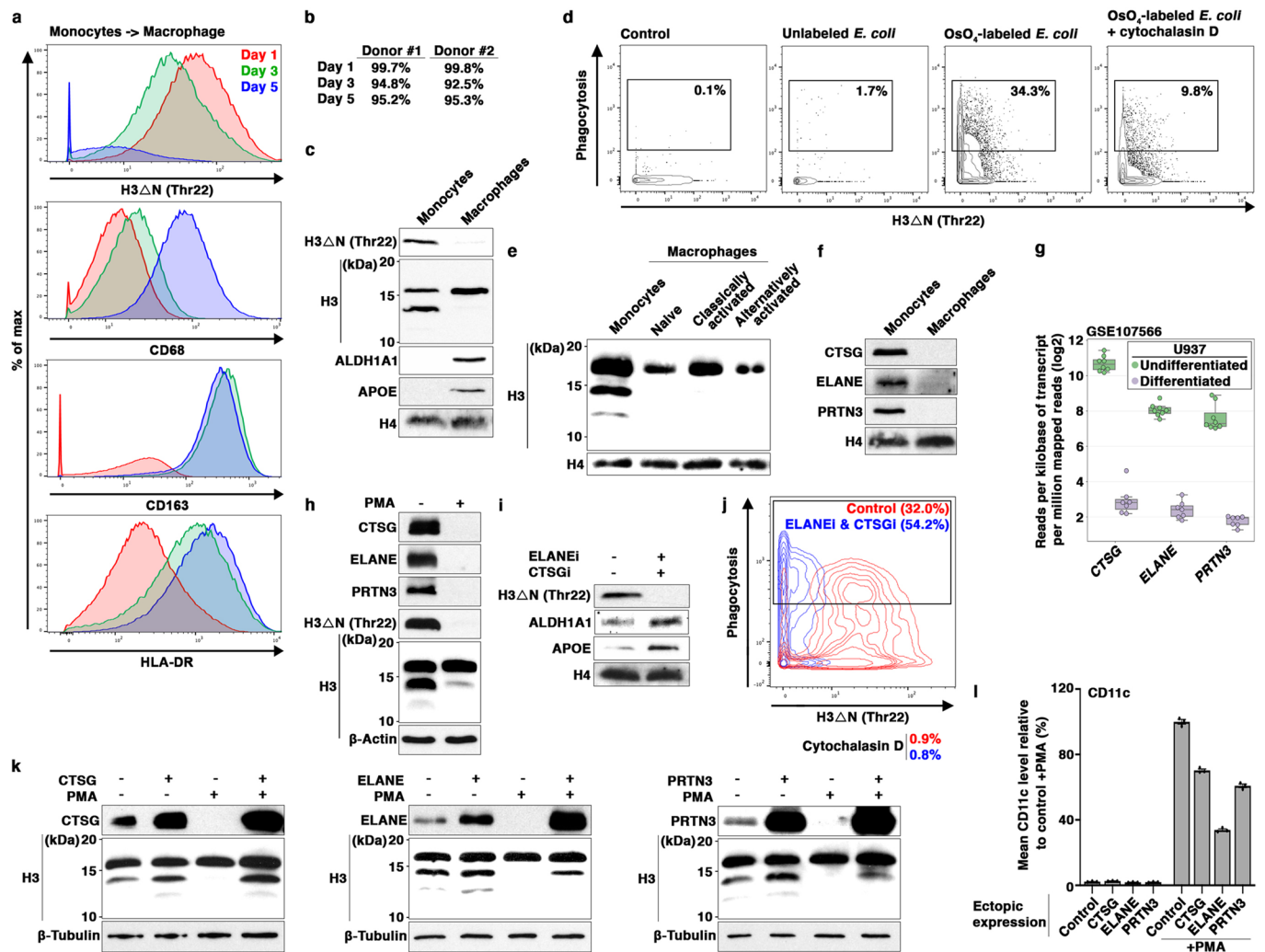
Extended Data Fig. 3 | NSP and H3ΔN Repression as Primary Monocytes Mature into Macrophages. a, H3ΔNThr22 repression during monocyte-to-macrophage differentiation. Mass cytometry analysis of monocytes and monocyte-derived macrophage. Cells collected at days one (red), three (green), and five (blue) in culture for differentiation are analyzed. Independent biological replicate of Fig. 3a from a different donor. **b**, H3ΔNThr22 repression during monocyte-to-macrophage differentiation is not associated with cell death. Viability of the cells as in Fig. 3a (donor 1) and (**a**) (donor 2) assessed by cisplatin staining and mass cytometry. **c**, Repression of all species of H3ΔN as monocytes differentiate into macrophages. Western blot analysis of WCE from primary monocytes and monocyte-derived macrophages. Macrophages, cells collected at day seven in culture. Molecular weight markers, see Source Data. Independent biological replicate of Fig. 3b from a different donor. **d**, Macrophages depleted of H3ΔNThr22 show robust phagocytosis capability. Mass cytometry analysis of mature macrophages as in (**a**) (five-day differentiation *in vitro*) incubated with osmium-labelled *E. coli* to measure phagocytosis capability. Control, no *E coli* particle. Cytochalasin D is used to demonstrate the specificity of phagocytosis measurement. H3ΔNThr22 (x-axis) and osmium (y-axis) levels measured by mass cytometry are shown. Independent biological replicate of Fig. 3c from a different donor. **e**, H3ΔN repression is maintained in polarized macrophages. Western blot analysis of freshly isolated monocytes, naïve, classically activated, and alternatively activated macrophages from a healthy volunteer. Independent biological replicate of Fig. 3d. **f**, CTSG, ELANE, and PRTN3 repression during monocyte-to-macrophage differentiation. Western blot analysis of the samples as in (**c**) using the indicated antibodies. Molecular weight markers, see Source Data. Independent biological replicate of Fig. 3e from a different donor. **g**, Transcriptional repression of *CTSG*, *ELANE*, and *PRTN3* in U937 cells treated with PMA. Differential gene expression analysis of *CTSG*, *ELANE*, and *PRTN3* (x-axis) in undifferentiated (green) and differentiated (purple) U937 cells using the publicly available dataset GSE107566. Each dot represents an independent sample. Y-axis, reads per kilobase per million mapped reads (RPKM). **h**, Repression of CTSG, ELANE, and PRTN3 proteins in U937 cells treated with PMA. Western blot analysis of WCE from U937 cells treated with or without PMA using the indicated antibodies. **i,j**, Pharmacological inhibition of NSPs accelerates macrophage development. Western blot analysis of WCE from peripheral blood monocytes cultured in the absence or presence of ELANE inhibitor GW311616 in combination with CTSG inhibitor CAS 429676–93-7 (**i**). Phagocytosis analysis of the cells as in (**i**) using mass cytometry and osmium-labeled *E. coli* (**j**). Independent biological replicate of Fig. 3g,h from a different donor. **k**, Exogenous NSP expression is unaffected by NSP repression during cellular differentiation. Western blot analysis of WCE from U937 cells stably expressing exogenous CTSG (left), ELANE (middle), or PRTN3 (right) under the control of a cytomegalovirus promoter treated with or without PMA to induce differentiation. Control, cells transduced with lentiviral vector only without a transgene. (**l**) Constitutive NSP expression suppresses cellular differentiation. Ectopic overexpression of the indicated NSPs (x-axis) in U937 cells treated with PMA. CD11c expression is determined by mass cytometry. Data represent mean ± S.E.M. (three technical replicates).
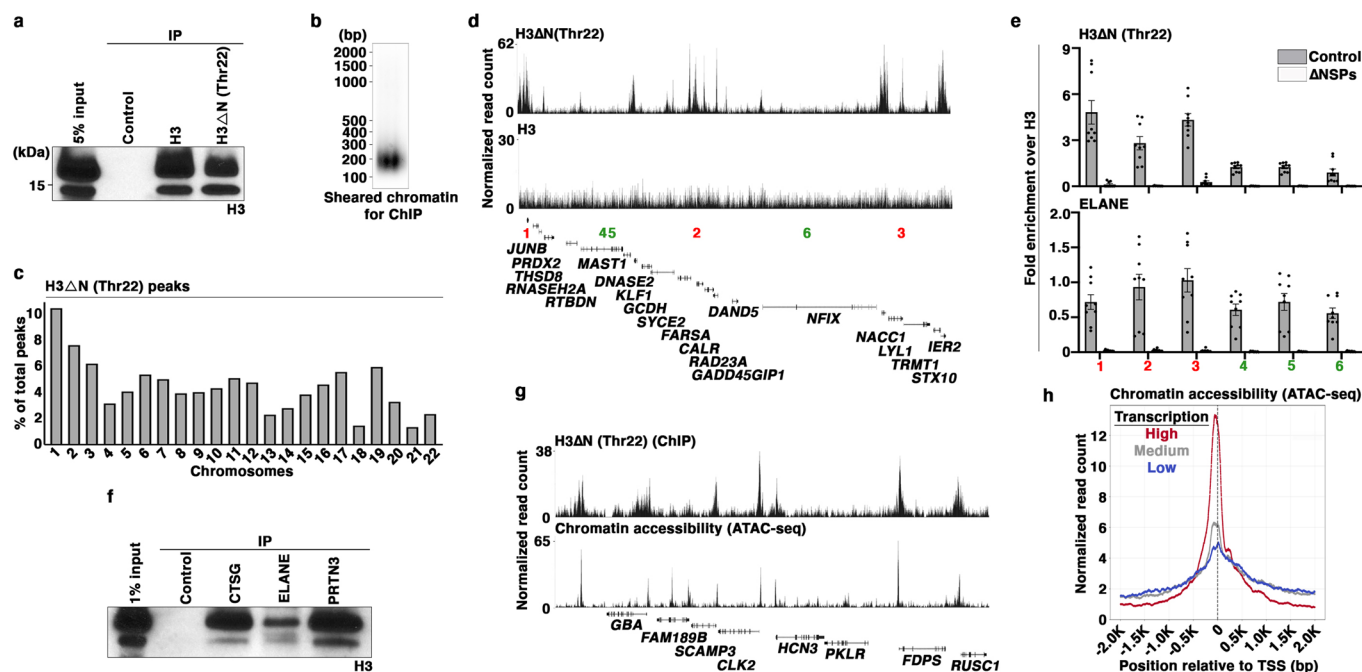
Extended Data Fig. 4 | Widespread H3ΔN Genomic Enrichment in Monocytic Cells is Associated with Permissive Chromatin and Active Transcription.
a, Validation of affinity reagents for ChIP-seq. Immunoprecipitation under the stringent ChIP condition using formaldehyde-crosslinked chromatin and the indicated antibodies. ChIP samples are subject to immunoblotting analysis using an antibody raised against H3. Control, bare magnetic beads.
b, Mono-nucleosome-enriched sheared chromatin for ChIP-seq analysis. Gel electrophoresis analysis of chromatin input for ChIP-seq analysis. DNA ladder in base pairs is shown. **c**, Widespread H3ΔNThr22 distribution across the genome. Percentages of H3ΔNThr22 peaks at the indicated 22 pairs of autosomes. **d,e**, Widespread H3ΔNThr22 enrichment and ELANE occupancy across the genome. Representative genomic tracks of H3ΔNThr22 (top) and bulk H3 (bottom) ChIP-seq data. Genomic regions with high (red) or low (green) H3ΔNThr22 ChIP-seq signals are tested (**d**). qPCR analysis of H3ΔNThr22 (top) or ELANE (bottom) ChIP DNA from control (gray) or ΔNSPs (white) cells using the indicated primer pairs. Y-axes, fold enrichment over bulk H3. Data represent mean ± S.E.M. (three biological replicates (three control cell lines or thee ΔNSPs clones) and three technical replicates (N = 9)) (**e**). **f**, Validation of affinity reagents for ChIP analysis of NSP occupancy. Immunoprecipitation as in (**a**) using antibodies recognizing the indicated NSPs. Immunoprecipitation samples are subsequently analyzed by immunoblotting using an antibody recognizing bulk H3. Control, bare magnetic beads.
g, Peak association between H3ΔNThr22 ChIP-seq and ATAC-seq datasets. Representative genomic tracks of H3ΔNThr22 ChIP-seq data from wild-type U937 cells (top) and ATAC-seq data from control cells (bottom). **h**, Positive correlation between transcriptional activity and chromatin accessibility. TSS-proximal ATAC-seq signals for the three groups of genes with high (red), medium (gray), or low (blue) gene expression activity (GSE107566).
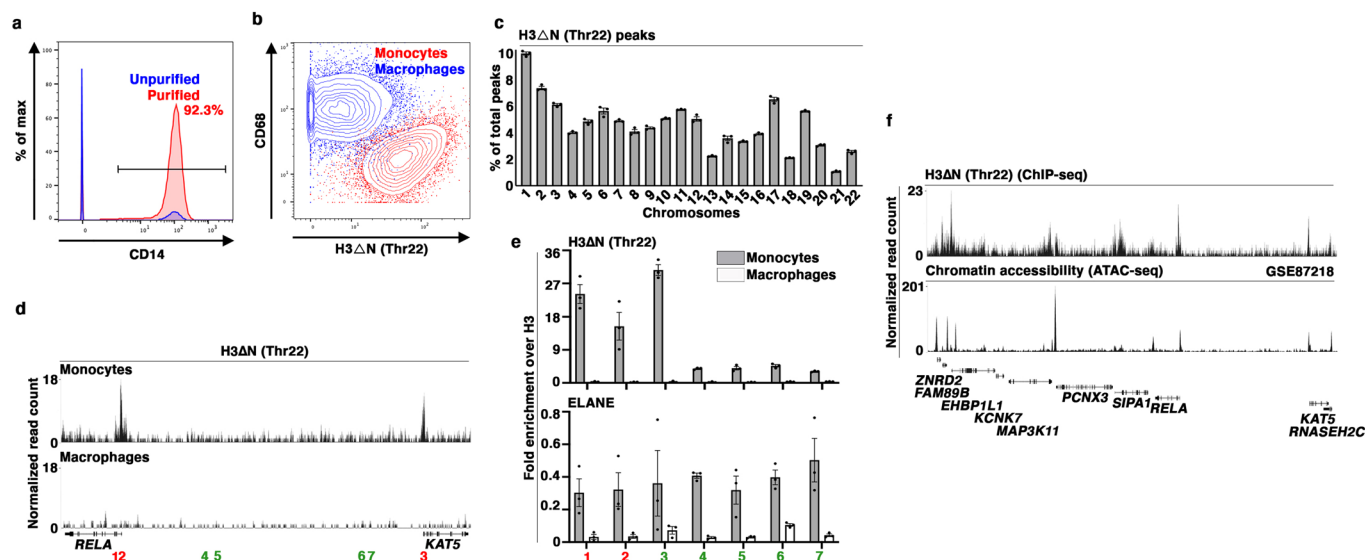
Extended Data Fig. 5 | Widespread H3ΔN Genomic Enrichment in Primary Monocytes is Associated with Permissive Chromatin and Active Transcription. Purity of primary monocytes used for ChIP-seq analysis. Representative mass cytometry data showing the percentages of CD14+ monocytes in bulk PBMC (blue) or purified monocyte samples (red) used for ChIP-seq analysis. X-axis, CD14 level; y-axis, percentage of the maximal count. **b**, Fully differentiated macrophages used for ChIP-seq analysis. Representative mass cytometry data showing H3ΔNThr22 (x-axis) level and CD68 expression (y-axis) in macrophages (blue) relative to those in monocytes (red) for the cells used for ChIP-seq analysis. **c**, Widespread H3ΔNThr22 distribution across the genome in primary monocytes. Percentages of H3ΔNThr22 peaks at the indicated 22 pairs of autosomes. Data represent mean ± S.E.M. (three biological replicates). **d,e**, H3ΔNThr22 enrichment and ELANE occupancy at the p65 subunit (*RELA*) of NF-κB locus in primary monocytes. Representative genomic tracks of H3ΔNThr22 ChIP-seq data from primary monocyte (top) or the matching monocyte-derived macrophages (bottom). Genomic regions with high (red) or low (green) H3ΔNThr22 are tested (**d**). qPCR analysis of H3ΔNThr22 enrichment (top) or ELANE occupancy (bottom) in primary monocytes (gray) or the matching macrophages (white) using the indicated primer pairs. Y-axes, fold enrichment over bulk H3. Data represent mean ± S.E.M. (three technical replicates) (**e**). **f**, H3ΔNThr22 is associated with permissive chromatin in primary monocytes. Representative genomic tracks of H3ΔNThr22 ChIP-seq (top) and ATAC-seq (GSE87218) (bottom) datasets from primary monocytes.
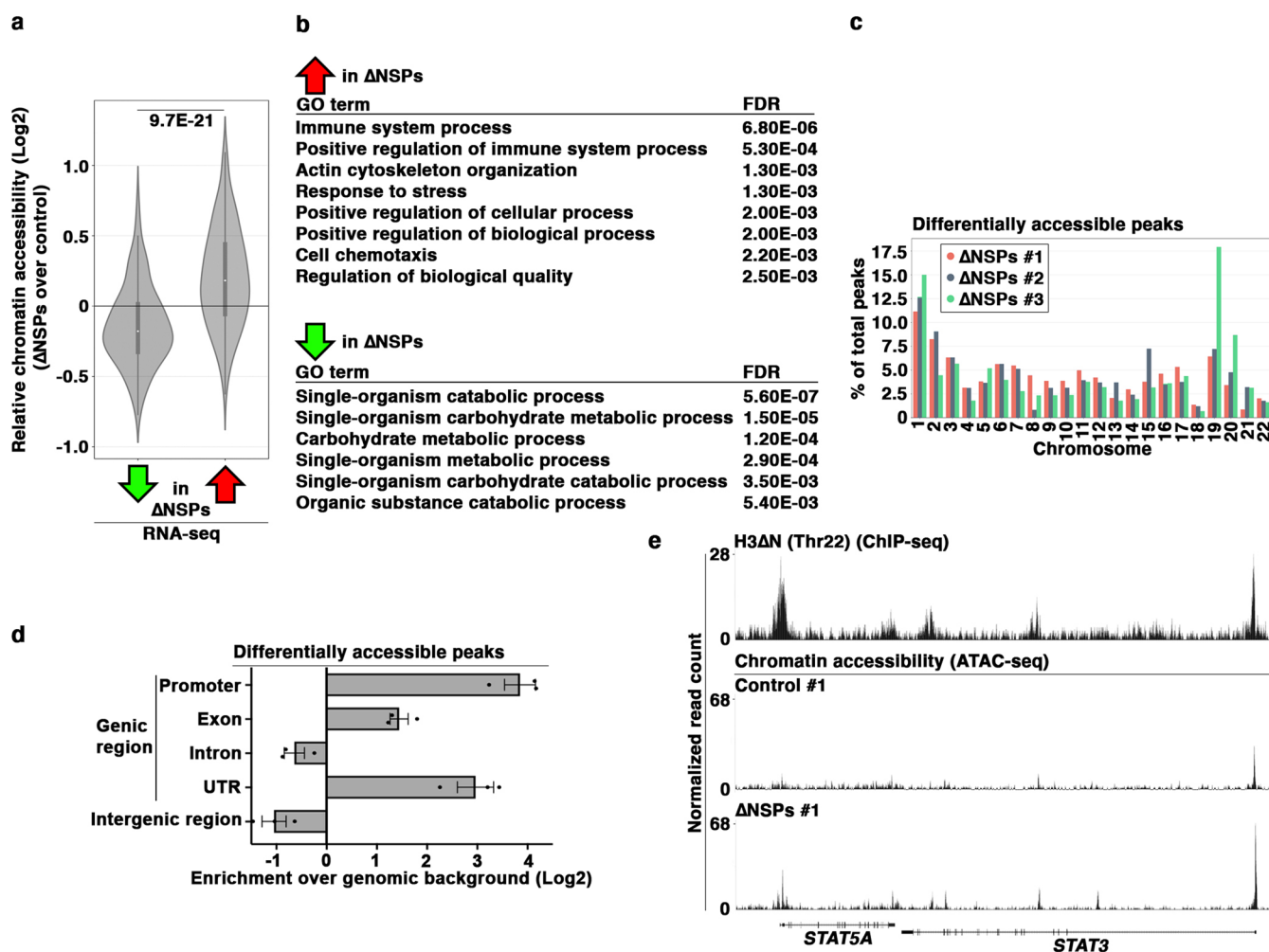
Extended Data Fig. 6 | NSP and H3ΔN Depletion Is Associated with Increased Chromatin Accessibility. a, Differential gene expression in ΔNSPs cells is associated with chromatin accessibility changes. Integrative analysis of ATAC-seq and RNA-seq datasets focusing on differentially expressed genes in Fig. 6a. Y-axis, relative chromatin accessibility determined by ATAC-seq; left, genes downregulated in ΔNSPs cells relative to controls (N = 220); right, genes upregulated in ΔNSPs cells relative to controls (N = 170). Statistical significance is determined by two-tailed Welch's *t* test with *P* value depicted. Differential gene expression in U937 cells depleted of NSPs affects selective biological processes. Gene ontology analysis of the differentially expressed genes in Fig. 6a. Gene ontology terms in which differential genes are enriched are ranked by FDR. **b**, Increased chromatin accessibility across the genome in U937 cells depleted of NSPs and H3ΔN. The distribution of differentially accessible peaks across 22 pairs of autosomes (x-axis) in ΔNSPs cells. Color, three independent ΔNSPs clones; y-axis, percentages of peaks at specific chromosomes. **c**, Genic region enrichment of differentially accessible peaks in ΔNSPs cells. X-axis, the presence of differentially accessible peaks in ΔNSPs cells in the indicated genomic regions over their relative proportions in the genome. Center line, genomic distribution with no enrichment. Data represent mean ± S.D. (three biological replicates). **d**, Further increase in chromatin accessibility upon NSP and H3ΔNThr22 depletion. Representative genomic tracks of the H3ΔNThr22 ChIP-seq dataset from wild-type U937 cells (top) and the ATAC-seq datasets from control (middle) or ΔNSPs (bottom) cells at the *STAT5A-STAT3* locus.
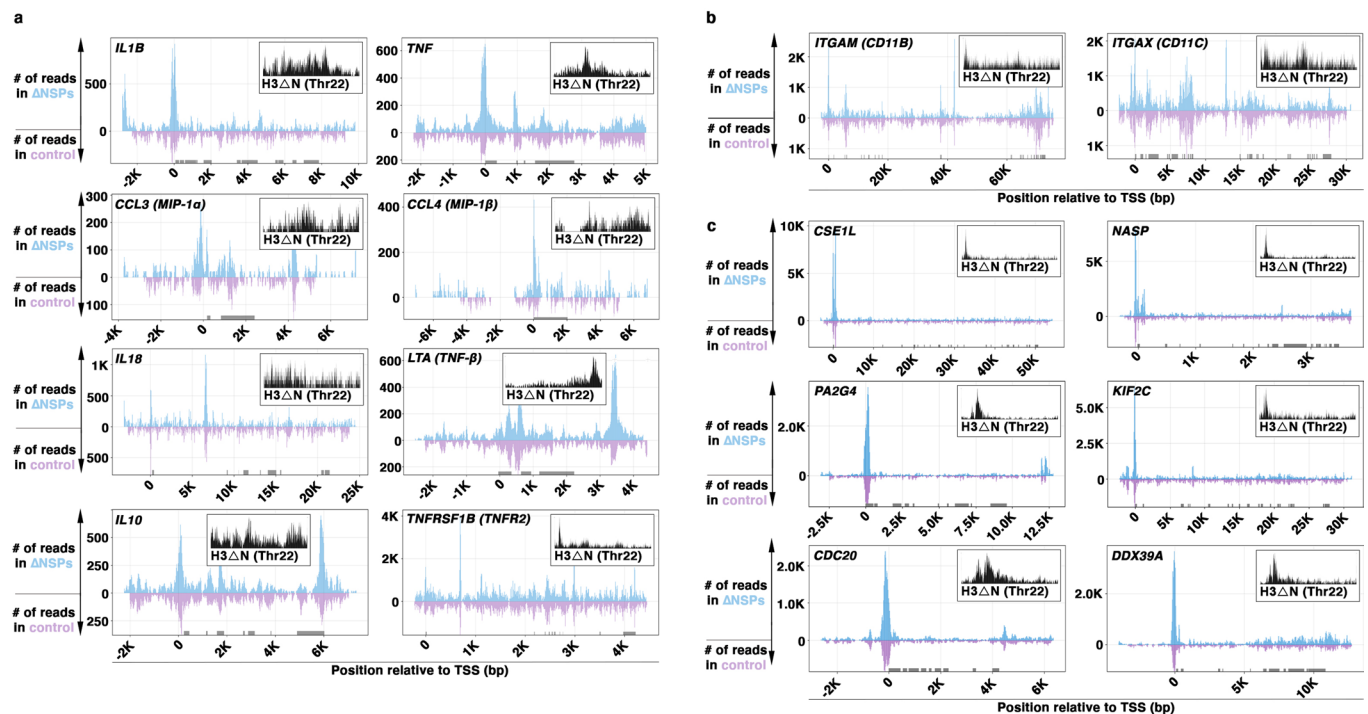
Extended Data Fig. 7 | NSP and H3ΔN Repression Primes the Chromatin to Facilitate Transcription Reprogramming During Cellular Differentiation.
a-c, Increased chromatin accessibility at genes with important immune regulatory functions in ΔNSPs cells. ATAC-seq sequencing tracks of the loci encoding proinflammatory cytokines, immune regulators (**a**), differentiation markers (**b**), or differential genes upon differentiation (**c**) in ΔNSPs (blue) or control (purple) cells. X-axis, relative position to TSS in base pairs; y-axis, normalized read count in ΔNSPs (above zero) or control (below zero) cells; gray block, exon. H3ΔNThr22 genomic track in wild-type U937 cells is shown.
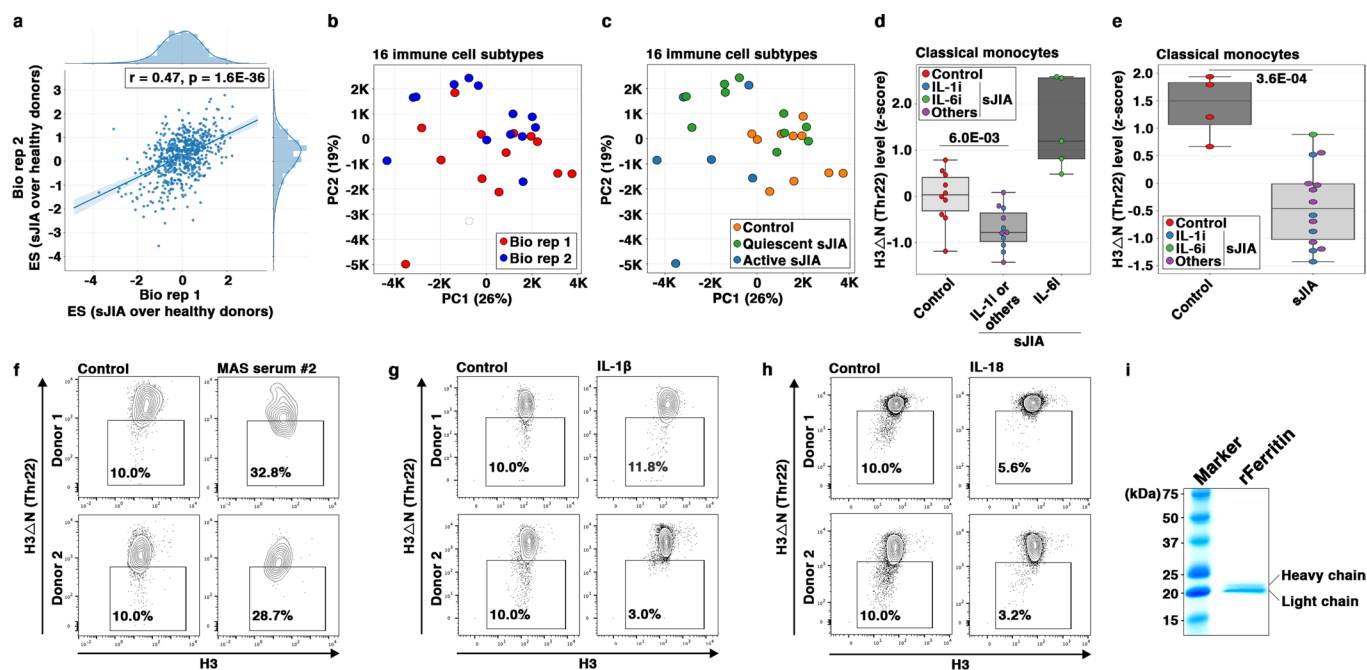
Extended Data Fig. 8 | IL-6 and Ferritin Contribute to H3ΔN Repression in Monocytes from sJIA patients. a, Robust epigenetic alterations in sJIA patients captured by independent replicates. EpiTOF analysis of the global levels of 40 histone marks in 16 major immune cell subtypes from sJIA patients and healthy volunteers. Effect size comparisons of 560 data points are computed using the biological replicates 1 (x-axis) or 2 (y-axis) datasets. The trendline and Pearson's correlation coefficient are shown. Statistical significance is determined by Student's t-test for Pearson correlation with P value depicted. **b**, Minimal batch effect between the two biological replicates. PCA of the EpiTOF data as in (**a**) where each dot represents a single subject from biological replicate 1 (red) or 2 (blue) using the variance of 40 histone marks in 16 major immune cell subtypes (560 data points). The proportion of the variance explained by each principal component is shown. **c**, Separation of sJIA patients from healthy volunteers by epigenetic landscape. PCA as in (**b**). Orange, healthy donors; green, sJIA patients with quiescent disease; blue, sJIA patients with active disease. **d**, Repressed H3ΔNThr22 in sJIA patients with the exception of those on IL-6-blocking therapy. Box plot representation of the H3ΔNThr22 levels in monocytes from healthy volunteers, sJIA patients on IL-1 (blue) or IL-6 targeting therapies (green), or on no or other biologic treatments (purple). Center line, median; box limits, upper and lower quartiles; whiskers, 1.5x interquartile range; points, outliers. Statistical significance is determined by two tailed Student's t-test with P value depicted. **e**, Reduced H3ΔNThr22 in monocytes from sJIA patients. EpiTOF analysis of PBMCs from 14 sJIA patients and 4 healthy volunteers focusing on H3ΔNThr22 in monocytes. An independent validation cohort in addition to the one described in Fig. 8a. Each dot represents the H3ΔNThr22 level in monocytes from a subject. sJIA patients are colored based on treatments as in (**d**). Center line, median; box limits, upper and lower quartiles; whiskers, 1.5x interquartile range; points, outliers. Statistical significance is determined by two tailed Student's t-test with P value depicted. **f**, Sera from sJIA patients with MAS induce H3ΔNThr22 repression in monocytes from healthy volunteers. Mass cytometry analysis of monocytes from two healthy volunteers (top and bottom) cultured *in vitro* with sera from a healthy donor (left) or a sJIA patient with MAS (right) for 24 hours. Biological replicate of the experiment described in Fig. 8f using independent serum sample from an sJIA patient with MAS and independent PBMCs from two healthy volunteers. **g,h**, Clinically important cytokines IL-1β and IL-18 do not induce H3ΔNThr22 repression in monocytes. Mass cytometry analysis of PBMCs from two healthy volunteers (top and bottom) treated with (right) or without (left) IL-1β (**g**) or IL-18 (**h**) for 24 hours. X-axis, bulk H3; y-axis, H3ΔNThr22 level; each dot represents a single monocyte. **i**, Purity of recombinant ferritin for *ex vivo* monocyte stimulation. Coomassie staining of ferritin complex purified from *E. coli* ectopically co-expressing the heavy and light subunits of ferritin. Molecular weight marker is shown.

nature research

Corresponding author(s): Elizabeth D. Mellins, Purvesh Khatri, Paul J. Utz, Alex J. Kuo

Last updated by author(s): Mar 26, 2021

Reporting Summary

Nature Research wishes to improve the reproducibility of the work that we publish. This form provides structure for consistency and transparency in reporting. For further information on Nature Research policies, see Authors & Referees and the Editorial Policy Checklist.

Statistics

For all statistical analyses, confirm that the following items are present in the figure legend, table legend, main text, or Methods section.

n/a	Confirmed	
☐	☒	The exact sample size (*n*) for each experimental group/condition, given as a discrete number and unit of measurement
☐	☒	A statement on whether measurements were taken from distinct samples or whether the same sample was measured repeatedly
☐	☒	The statistical test(s) used AND whether they are one- or two-sided *Only common tests should be described solely by name; describe more complex techniques in the Methods section.*
☐	☒	A description of all covariates tested
☐	☒	A description of any assumptions or corrections, such as tests of normality and adjustment for multiple comparisons
☐	☒	A full description of the statistical parameters including central tendency (e.g. means) or other basic estimates (e.g. regression coefficient) AND variation (e.g. standard deviation) or associated estimates of uncertainty (e.g. confidence intervals)
☐	☒	For null hypothesis testing, the test statistic (e.g. *F*, *t*, *r*) with confidence intervals, effect sizes, degrees of freedom and *P* value noted *Give P values as exact values whenever suitable.*
☒	☐	For Bayesian analysis, information on the choice of priors and Markov chain Monte Carlo settings
☒	☐	For hierarchical and complex designs, identification of the appropriate level for tests and full reporting of outcomes
☐	☒	Estimates of effect sizes (e.g. Cohen's *d*, Pearson's *r*), indicating how they were calculated

Our web collection on statistics for biologists contains articles on many of the points above.

Software and code

Policy information about availability of computer code

Data collection	Relevant software used for data collection: EpiTOF data - FlowJo (v. 10.6.1) Sequencing data - FastQ files generated by third party sequencing service company
Data analysis	Data preprocessing (e.g. alignment, peak calling) for sequencing data was carried out using: Bowtie2 (v2.3.4.1) for alignment of ATAC-Seq and ChIP-Seq data, HISAT2 for alignment of RNA-Seq data, Skewer (v0.2.2) for adapter trimming, FastQC (v0.11.7) for QC, Picard Tools (v2.18.0) for deduplication, MACS2 (v2.2.7.1) for peak calling. All steps prior to peak calling were carried out using the PEPATAC pipeline (v0.8.3; http://code.databio.org/PEPATAC/) All data analysis after preprocessing was conducted in Python (v. 3.6.4) using the following packages: Pandas (v. 0.23.4), statsmodels (v. 0.8.0), matplotlib (v. 2.2.2), Seaborn (v. 0.9.0)

For manuscripts utilizing custom algorithms or software that are central to the research but not yet described in published literature, software must be made available to editors/reviewers. We strongly encourage code deposition in a community repository (e.g. GitHub). See the Nature Research guidelines for submitting code & software for further information.

Data

Policy information about availability of data

All manuscripts must include a data availability statement. This statement should provide the following information, where applicable:

- Accession codes, unique identifiers, or web links for publicly available datasets
- A list of figures that have associated raw data
- A description of any restrictions on data availability

ATAC-seq, ChIP−seq, and RNA-seq datasets have been deposited in the Gene Expression Omnibus with accession numbers GSE142660, GSE142661, and GSE142662, respectively. All raw data and source data that support the findings of this study are available from the corresponding authors upon request.

Field-specific reporting

Please select the one below that is the best fit for your research. If you are not sure, read the appropriate sections before making your selection.

☒ Life sciences ☐ Behavioural & social sciences ☐ Ecological, evolutionary & environmental sciences

For a reference copy of the document with all sections, see nature.com/documents/nr-reporting-summary-flat.pdf

Life sciences study design

All studies must disclose on these points even when the disclosure is negative.

Sample size	For the analyses related to sJIA samples, a preliminary unpublished dataset on H3DT22 levels in sJIA patients suggested marked decrease in H3DT22 level in sJIA relative to that in healthy subjects with effect sizes <-1. Using this estimate, a power analysis assuming an unpaired one-tailed t-test at 80% power, effect size -1, and significance level 0.05 was performed. The analysis suggested that a sample size greater than 13 is required. We were able to obtain clinical samples from 16 patients with sJIA. For analyses related to the sJIA serum, no statistical method was used to predetermine sample size. The design was based on the number of samples that can be barcoded for combined mass cytometry processing and analysis to minimize technical variability.
Data exclusions	No data were excluded.
Replication	For ChIP-seq, we analyzed wild-type U937 cells in two biological replicates. ChIP-seq analysis of H3DT22 was performed on three primary monocyte samples and their matching monocyte-derived macrophages. ATAC-seq and RNA-seq were employed to analyze three DNSPs clones and control cell lines. All other experiments described in the manuscripts were repeated at least 2 times. All replicates were successful.
Randomization	Samples from patients with quiescent or active sJIA were randomly assigned and analyzed in two biological replicates. Samples from healthy volunteers were obtained from Stanford Blood Center with age being the only selection criterion (between 17 and 18). All samples were randomly assigned to different experimental groups. For other analyses, the experiments were not randomized.
Blinding	All measurements were objectively quantifiable (e.g. instrument output). Thus, blinding was not applicable.

Reporting for specific materials, systems and methods

We require information from authors about some types of materials, experimental systems and methods used in many studies. Here, indicate whether each material, system or method listed is relevant to your study. If you are not sure if a list item applies to your research, read the appropriate section before selecting a response.

Materials & experimental systems

n/a	Involved in the study
☐	☒ Antibodies
☐	☒ Eukaryotic cell lines
☒	☐ Palaeontology
☒	☐ Animals and other organisms
☐	☒ Human research participants
☒	☐ Clinical data

Methods

n/a	Involved in the study
☐	☒ ChIP-seq
☐	☒ Flow cytometry
☒	☐ MRI-based neuroimaging

Antibodies

Antibodies used	CD16-209Bi 3G8 (Fluidigm #3209002B), 1ul/test per the manufacturer's recommendation Acetylated-Lysine RM101 (RevMab #32101200), 0.5ug/test CD11b ICRF44 (BioLegend #301337), 0.5ug/test Alexa 647 CD19 HIB19 (BioLegend #302220), 5ul/test per the manufacturer's recommendation PE/Cy7 CD3 UCHT1 (BioLegend #300420), 5ul/test per the manufacturer's recommendation FITC CD45 HI30 (BioLegend 304038), 5ul/test per the manufacturer's recommendation PE CD14 M5E2 (BioLegend #304038), 5ul/test per the manufacturer's recommendation H3 (abcam #1791), 1:5000 dilution H3 Cleaved Thr22 (Cell Signaling Technology #12576), 1:1000 dilution CTSG (abcam #49854), 1:2000 dilution PRTN3 EPR6277 (abcam,#133613), 1:1000 dilution ELANE EPR7479 (abcam #21595), 1:1000 dilution Apolipoprotein EP1374Y (abcam #52607), 1:1000 dilution ALDH1A1 (abcam #227948), 1:1000 dilution H4 31830 (abcam #31830), 1:2000 dilution beta-actin D6A8 (Cell Signaling Technology #8457L), 1:1000 dilution beta-tubulin 9F3 (Cell Signaling Technology #2128), 1:1000 dilution Cathepsin L+V 33/2 (abcam #6314), 1:1000 dilution FLAG Tag 9A3 (Cell Signaling Technology #8146), 1:2000 dilution Other antibodies used for mass cytometry have been described previously (PMID: 29706550).
Validation	The cleaved H3 Thr22 antibody used throughout the study has been validated using synthetic peptides and immunoblotting (Extended Data Fig. 2d). Antibodies against NSPs were validated in Extended Data Fig. 2a, 2b, 2c, and 3k. All other antibodies for mass cytometry were validated previously (PMID: 29706550).

Eukaryotic cell lines

Policy information about cell lines

Cell line source(s)	U-937 (ATCC), THP-1 (ATCC), Jurkat (ATCC), OCI-Lys3 (DSMZ).
Authentication	All cell lines showed phenotypic and morphologic characteristics in culture as expected upon receipt from ATCC or DSMZ. Upon any observance of changes during routine culture, and at periodic intervals of no longer than 6 months of active use, the cell lines were re-authenticated using short tandem repeat (STR) profiling (https://www.atcc.org/en/Services/).
Mycoplasma contamination	Negative by MycoAlert Mycoplasma Detection Kit (Lonza, LT07-118).
Commonly misidentified lines (See ICLAC register)	None was used in this study.

Human research participants

Policy information about studies involving human research participants

Population characteristics	Related to sJIA analysis in Figure 8. clinical samples were collected at four institutions, including Stanford Children's Hospital, Cincinnati Children's Hospital, University of California San Francisco, and Boston Children's Hospital. The patients were separated into two biological replicates with comparable population characteristics (e.g. age, sex, and disease activity) Active disease: presence of systemic features including fever, rash, adenopathy or hepatosplenomegaly, and elevated erythrocyte sedimentation rate (ESR) and C-reactive protein (CRP) and/or active arthritis. Quiescent disease: absence of the symptoms of active disease and normal ESR and CRP. Randomly assigned: age, between 3 and 17 (median: 11); Sex, 12 female and 4 male; genotype, not determined.; biologic treatments, listed in Supplementary Table 1. Healthy volunteers were recruited at Stanford Blood Center. Randomly assigned: age, between 17 and 18 (median: 17); Sex, 5 female and 5 male; genotype, not determined.
Recruitment	Clinical samples were selected from the sJIA biobanks at the institutions above. Disease activity was the only criterion used for sample selection.
Ethics oversight	Stanford University IRB (protocols 13932 and 13942); The IRB of Boston Children's Hospital (protocols IRB P00005723 and 07-09-0375); The IRB of Cincinnati Children's Hospital Medical Center (IRB 2016-2234); University of California San Francisco IRB (13-10826).

Note that full information on the approval of the study protocol must also be provided in the manuscript.

ChIP-seq

Data deposition

☒ Confirm that both raw and final processed data have been deposited in a public database such as [GEO](#).

☒ Confirm that you have deposited or provided access to graph files (e.g. BED files) for the called peaks.

Data access links
May remain private before publication.

GSE142661

Files in database submission

GEO Accession Numbers and Descriptions :
GSM4837221 Bulk H3_rep1
GSM4837222 H3ΔNThr22_rep1
GSM4837223 Bulk H3_rep2
GSM4837224 H3ΔNThr22_rep2
GSM4837225 Bulk H3_primary monocyte_donor1
GSM4837226 H3ΔNThr22_primary monocyte_donor1
GSM4837227 Bulk H3_primary monocyte_donor2
GSM4837228 H3ΔNThr22_primary monocyte_donor2
GSM4837229 Bulk H3_primary monocyte_donor3
GSM4837230 H3ΔNThr22_primary monocyte_donor3
GSM4837231 Bulk H3_monocyte-derived macrophages_donor1
GSM4837232 H3ΔNThr22_monocyte-derived macrophages_donor1
GSM4837233 Bulk H3_monocyte-derived macrophages_donor2
GSM4837234 H3ΔNThr22_monocyte-derived macrophages_donor2
GSM4837235 Bulk H3_monocyte-derived macrophages_donor3
GSM4837236 H3ΔNThr22_monocyte-derived macrophages_donor3

BigWig File Names:
Bulk_H3_monocyte_derived_macrophages_donor1.bw
Bulk_H3_monocyte_derived_macrophages_donor2.bw
Bulk_H3_monocyte_derived_macrophages_donor3.bw
Bulk_H3_primary_monocytes_donor1.bw
Bulk_H3_primary_monocytes_donor2.bw
Bulk_H3_primary_monocytes_donor3.bw
Bulk_H3_rep1.bw
Bulk_H3_rep2.bw
H3dNThr22_monocyte_derived_macrophages_donor1.bw
H3dNThr22_monocyte_derived_macrophages_donor2.bw
H3dNThr22_monocyte_derived_macrophages_donor3.bw
H3dNThr22_primary_monocytes_donor1.bw
H3dNThr22_primary_monocytes_donor2.bw
H3dNThr22_primary_monocytes_donor3.bw
H3dNThr22_rep1.bw
H3dNThr22_rep2.bw

Genome browser session
(e.g. [UCSC](#))

https://www.genome.ucsc.edu/s/schaffert/hg38%09h3t22_chip_with_primary

Methodology

Replicates

Wild-type U937 cells, two biological replicates; primary monocytes and the matching monocyte-derived macrophages from three healthy donors.

Sequencing depth

All reads are paired-end.

Aligned_reads_human_repeats = Reads aligned to human repeats
Aligned_reads = Reads aligned to non-repeats (used in downstream analysis)

Sample	Raw_reads	Aligned_reads_human_repeats	Aligned_reads	length
Bulk_H3_monocyte_derived_macrophages_donor1	51102848	1972104	19707748	101
Bulk_H3_monocyte_derived_macrophages_donor2	87399476	3716646	40588814	101
Bulk_H3_monocyte_derived_macrophages_donor3	90774470	3985222	47072210	101
H3dNThr22_monocyte_derived_macrophages_donor1	24363910	811140	11992228	101
H3dNThr22_monocyte_derived_macrophages_donor2	66153394	2326736	32706098	101
H3dNThr22_monocyte_derived_macrophages_donor3	41694324	1211122	17697080	101
Bulk_H3_primary_monocytes_donor1	33844386	1446650	14572746	101
Bulk_H3_primary_monocytes_donor2	63579444	3077256	33749426	101
Bulk_H3_primary_monocytes_donor3	127164320	6207008	65193708	101
H3dNThr22_primary_monocytes_donor1	67922896	2707950	37373336	101
H3dNThr22_primary_monocytes_donor2	36472544	1144222	19831540	101

H3dNThr22_primary_monocytes_donor3	77595338	2783368	44348778	101
Bulk_H3_rep1	124234822	6782586	78399876	101
Bulk_H3_rep2	41694324	1211122	17697080	101
H3dNThr22_rep1	93254160	3867974	66605992	101
H3dNThr22_rep2	98548504	3467500	66927292	101

Antibodies	H3 (abcam, #1791), H3 Cleaved Thr22 (Cell Signaling Technology, #12576)
Peak calling parameters	Alignment: Reads were aligned to human repeats (https://github.com/databio/ref_decoy) and mitochondrial DNA (http://www.ncbi.nlm.nih.gov/nuccore/251831106) using bowtie2 with the following parameters: -p 30 -k 1 -D 20 -R 3 -N 1 -L 20 -i S,1,0.50 Remaining unaligned reads were aligned to the human genome (GRCh38) using bowtie2 with the following parameters: -p 30 --very-sensitive -X 2000 Duplicates were removed using Picard tools with the following parameters: VALIDATION_STRINGENCY=LENIENT. Peaks were then called using MACS2 callpeak using the following parameters: -f BAMPE -q 0.25 --call-summits --nomodel --keep-dup all. The comparison/control (-c) parameter was supplied with the input sample.
Data quality	Number of Peaks with FDR < 5% in H3dNThr22 samples: H3dNThr22_monocyte_derived_macrophages_donor1 0 H3dNThr22_monocyte_derived_macrophages_donor2 290 H3dNThr22_monocyte_derived_macrophages_donor3 1 H3dNThr22_primary_monocytes_donor1 6348 H3dNThr22_primary_monocytes_donor2 10309 H3dNThr22_primary_monocytes_donor3 15661 H3dNThr22_rep1 59883 H3dNThr22_rep2 38776
Software	All data processing was carried out using a modified PEPATAC pipeline (http://code.databio.org/PEPATAC/) version 0.8.6, where the MACS2 parameters were modified for ChIP-seq and ATAC-seq specific features like TSS plots were not generated.

Flow Cytometry

Plots

Confirm that:

☒ The axis labels state the marker and fluorochrome used (e.g. CD4-FITC).

☒ The axis scales are clearly visible. Include numbers along axes only for bottom left plot of group (a 'group' is an analysis of identical markers).

☒ All plots are contour plots with outliers or pseudocolor plots.

☒ A numerical value for number of cells or percentage (with statistics) is provided.

Methodology

Sample preparation	See Methods and PMID: 29706550
Instrument	Mass Cytometer (CyTOF-Helios) (Fluidigm).
Software	FlowJo 10.6.2
Cell population abundance	(Classical) monocytes were defined as CD3-CD56-MHC-II+CD19-CD14+CD16-.
Gating strategy	See Methods and PMID: 29706550

☒ Tick this box to confirm that a figure exemplifying the gating strategy is provided in the Supplementary Information.